

ε Indi Ba, Bb: a detailed study of the nearest known brown dwarfs^{★,★★}

R. R. King¹, M. J. McCaughrean^{1,2}, D. Homeier³, F. Allard⁴, R.-D. Scholz⁵, and N. Lodieu⁶

¹ School of Physics, University of Exeter, Stocker Road, Exeter EX4 4QL, UK
e-mail: rob@astro.ex.ac.uk

² Research & Scientific Support Department, ESA ESTEC, Keplerlaan 1, 2200 AG Noordwijk, The Netherlands

³ Institut für Astrophysik, Georg-August-Universität, Friedrich-Hund-Platz 1, 37077 Göttingen, Germany

⁴ Centre de Recherche Astrophysique de Lyon, UMR 5574: CNRS, Université de Lyon, École Normale Supérieure de Lyon, 46 allée d'Italie, 69364 Lyon Cedex 07, France

⁵ Astrophysikalisches Institut Potsdam, An der Sternwarte 16, 14482 Potsdam, Germany

⁶ Instituto de Astrofísica de Canarias, vía Láctea s/n, 38200 La Laguna, Tenerife, Spain

Received 24 July 2009 / Accepted 6 November 2009

ABSTRACT

The discovery of ε Indi Ba, Bb, a binary brown dwarf system very close to the Sun, makes possible a concerted campaign to characterise the physical parameters of two T dwarfs. Recent observations suggest substellar atmospheric and evolutionary models may be inconsistent with observations, but there have been few conclusive tests to date. We therefore aim to characterise these benchmark brown dwarfs to place constraints on such models. We have obtained high angular resolution optical, near-infrared, and thermal-infrared imaging and medium-resolution (up to $R \sim 5000$) spectroscopy of ε Indi Ba, Bb with the ESO VLT and present *VRIzJHKL'M'* broad-band photometry and 0.63–5.1 μm spectroscopy of the individual components. The photometry and spectroscopy of the two partially blended sources were extracted with a custom algorithm. Furthermore, we use deep AO-imaging to place upper limits on the (model-dependent) mass of any further system members. We derive luminosities of $\log L/L_{\odot} = -4.699 \pm 0.017$ and -5.232 ± 0.020 for ε Indi Ba, Bb, respectively, and using the dynamical system mass and COND03 evolutionary models predict a system age of 3.7–4.3 Gyr, in excess of previous estimates and recent predictions from observations of these brown dwarfs. Moreover, the effective temperatures of 1352–1385 K and 976–1011 K predicted from the COND03 evolutionary models, for ε Indi Ba and Bb respectively, are in disagreement with those derived from the comparison of our data with the BT-Settl atmospheric models where we find effective temperatures of 1300–1340 K and 880–940 K, for ε Indi Ba and Bb respectively, with surface gravities of $\log g = 5.25$ and 5.50. Finally, we show that spectroscopically determined effective temperatures and surface gravities for ultra-cool dwarfs can lead to underestimated masses even where precise luminosity constraints are available.

Key words. stars: atmospheres – stars: fundamental parameters – stars: brown dwarfs – stars: individual: ε Indi B – binaries: general – stars: late-type

1. Introduction

The characterisation of low-mass stars and brown dwarfs is important for studies of substellar and planetary atmospheres, the reliable application of low-mass evolutionary models, and the derivation of the full initial mass function. With over five hundred L and over one hundred T dwarfs now known¹, statistical studies of global properties and detailed studies of the closest objects are now possible.

Binary systems have an important role to play. They allow the determination of dynamical masses, provide a laboratory in which objects with the same age and chemical composition may be compared, and, where they have main-sequence companions,

provide external constraints of metallicity and age which isolated objects lack, breaking the substellar mass-luminosity-age degeneracy.

To fully constrain the evolutionary models of substellar objects (e.g. Burrows et al. 1997; Baraffe et al. 2003; Saumon & Marley 2008), it would be most useful to determine the bolometric luminosity, radius, mass, and age of a range of such objects. Bolometric luminosities can be determined from photometric and spectroscopic observations across a large wavelength range. Masses can be determined in systems where an orbit may be monitored, and finally, the age and metallicity can be inferred from better characterised stars in the same system. To constrain the atmospheric models of brown dwarfs, it is necessary to acquire high signal-to-noise spectra over as wide a wavelength range as possible, allowing robust estimates of the effective temperature and surface gravity to be made.

The discovery of a distant companion (projected separation ~ 1500 AU) to the high proper-motion (~ 4.7 arcsec/yr) K4.5V star, ε Indi, was reported by Scholz et al. (2003). One of our nearest neighbours, ε Indi A has a well-constrained parallax from HIPPARCOS (Perryman & ESA 1997) as refined by van Leeuwen (2007), putting the system at a distance of

[★] Based on observations collected with the ESO VLT, Paranal, Chile under program 072.C-0689

^{★★} The full resolution spectra of both brown dwarfs are only available in electronic form at the CDS via anonymous ftp to cdsarc.u-strasbg.fr (130.79.128.5) or via <http://cdsweb.u-strasbg.fr/cgi-bin/qcat?J/A+A/510/A99>

¹ <http://dwarfarchives.org> – the M, L, and T dwarf compendium maintained by Chris Gelino, Davy Kirkpatrick, and Adam Burgasser.

3.6224 ± 0.0037 pc. This was followed by the discovery of the companion's binary nature (McCaughrean et al. 2004). The proximity of ε Indi Ba, Bb to the Earth means Ba is more than a magnitude brighter than any other known T dwarf, and allows unprecedented, detailed spectroscopic studies of these important template objects.

ε Indi Ba, Bb are uniquely suited to provide key insights into the physics, chemistry, and evolution of substellar sources. Although there are a number of other T dwarfs in binary systems, such as the M4/T8.5 binary Wolf 940 (Burningham et al. 2009) and the T5/T5.5 binary 2MASS 1534–2952 (Liu et al. 2008), ε Indi Ba, Bb has a very well-determined distance, a main-sequence primary star with which to constrain age and metallicity, and a short enough orbit (nominally ~15 years, McCaughrean et al. 2004) such that the system and individual dynamical masses can soon be determined (McCaughrean et al.; Cardoso et al., in prep.). They are also relatively bright, close enough, and sufficiently separated to allow detailed photometric and spectroscopic studies of both components. Importantly, these two objects roughly straddle the L to T transition (cf. Burgasser 2009) where the atmospheres of substellar objects alter dramatically. The study of these two coeval objects on either side of the transition will help in understanding the processes effecting the change from cloudy to cloud-free atmospheres. Characterisation of this system allows the mass-luminosity-age relation at low masses and intermediate age to be tested, investigation of the atmospheric chemistry, including vertical up-mixing, and detailed investigation of the species in the atmosphere.

To date, spectroscopic observations of T dwarfs have predominantly been either at low-resolution (e.g., Burgasser et al. 2002; Chiu et al. 2006), which allows spectral classification and overall spectral energy distribution modelling to determine luminosities, or high-resolution studies of relatively small wavelength regions to investigate gravity and effective temperature-sensitive features. For example, McLean et al. (2003) presented near-IR spectra at a spectral resolution of $R \sim 2000$ of objects spanning spectral types M6 to T8, and discussed broad changes in spectral morphology and dominant absorbers through the spectral sequence. This was complemented by $R \sim 20000$ J -band spectra presented in McLean et al. (2007) where many H₂O and FeH features were identified and the progression of the J -band potassium doublet from M to T dwarfs charted.

Previous studies of ultra-cool dwarfs attempting to constrain low-mass evolutionary models have been hampered by ambiguous ages, possible unresolved binarity, and the difficulty associated with acquiring observations of close, faint companions. For example, observations of AB Dor C have roused some controversy over the applicability of current low-mass evolutionary models, with the assumed age of the system being a major source of disagreement. Close et al. (2005) determined a dynamical mass for AB Dor C and, using an assumed age of 30–100 Myr, argued that evolutionary models predicted a higher luminosity than was observed. However, Luhman et al. (2005) countered with an analysis based on an age of 75–150 Myr, finding no significant discrepancy between the observations and models. Nielsen et al. (2005) further argued that using their slightly revised age of 70 ± 30 Myr, the models still under-estimated the mass of this object. Again, this was disputed by Luhman & Potter (2006) after a re-reduction of the same data used by Close et al. (2005), and then Close et al. (2007) concluded that, based on newly acquired spectra, there was no discrepancy between the observations and models. Despite this apparent rapprochement,

the situation may nevertheless be further complicated by the suggestion of Marois et al. (2005) that AB Dor C may itself be an unresolved binary. More recently, Dupuy et al. (2009) presented a dynamical mass for the binary L dwarf system HD 130948BC which, along with an age estimated from the rotation of the main-sequence parent star, suggests that the evolutionary models predict luminosities 2–3 times higher than those observed.

Leggett et al. (2008) used 0.8–4.0 μm spectra at $R \sim 100$ –460 and near- to mid-IR photometry of HN Peg B, a T2.5 dwarf companion to a nearby G0V star, to investigate physical properties including dust grain properties and vertical mixing. In the near-IR, the resolution was too low to study spectral lines in detail. However, by fitting the overall spectral morphology and making use of the longer-wavelength data, they were able to place important constraints on vertical mixing and sedimentation. Leggett et al. (2009) also reported the physical properties of four T8–9 dwarfs from fitting observed near- to mid-IR spectral energy distributions with the atmospheric and evolutionary models of Saumon & Marley (2008). They discussed the effects of vertical transport of CO and N₂ and demonstrated the complementary effects of increasing metallicity and surface gravity.

Reiners et al. (2007) analysed high-resolution ($R \sim 33\,000$) optical spectra of three L dwarfs and the combined ε Indi Ba, Bb system, concluding that although some individual features are not well-matched by the model atmospheres and that significant differences remain for some molecular species and alkali metal features, general features are reproduced. Smith et al. (2003) also acquired high resolution ($R \sim 50\,000$) near-IR spectra of (only) ε Indi Ba in the wavelength ranges 1.553–1.559 μm and 2.308–2.317 μm . These were fit with the unified cloud models of Tsuji (2002) and effective temperatures of 1400 K and 1600 K were derived for the two spectral regions. Mid-IR spectroscopy of the unresolved ε Indi Ba, Bb system was also acquired by Roellig et al. (2004), who use evolutionary models along with the luminosities of McCaughrean et al. (2004) and an assumed age of 0.8–2.0 Gyr to derive effective temperatures and surface gravities and then compared composite spectral models to the observed spectrum. Their predictions were revised by Mainzer et al. (2007) who derived effective temperatures of 1210–1250 K and 840 K, for ε Indi Ba and Bb respectively, under the assumption of a system age of ~1 Gyr.

Finally, Kasper et al. (2009) presented $R \sim 400$ near-IR NACO/VLT spectroscopy of ε Indi Ba, Bb which were compared to the evolutionary models of Burrows et al. (1997) and the atmospheric models of Burrows et al. (2006). They derived effective temperatures of 1250–1300 K and 875–925 K, and surface gravities of $\log g$ (cm s⁻¹) 5.2–5.3 and 4.9–5.1, for ε Indi Ba and Bb respectively, by comparing their observed spectra with their spectral models scaled using the distance and a radius predicted by their evolutionary models. We will discuss these results further in Sect. 10 in contrast to our new data.

In this paper we present high signal-to-noise photometry from the V - to M' -band (0.5–4.9 μm) and medium resolution spectroscopy from 0.6–5.1 μm of the individual components of the ε Indi Ba, Bb system. In Sect. 2, we describe the observations and data reduction, including the routines employed to extract the partially-blended photometry and spectroscopy. We re-derive the spectral types of both objects according to the updated classification scheme of Burgasser et al. (2006b) in Sect. 3 and discuss constraints imposed by the parent main-sequence star in Sect. 4. We derive the luminosities of both sources in Sect. 5 and discuss the preliminary dynamical mass measurement of McCaughrean et al. (in prep.) in Sect. 6. Our observations are compared to

evolutionary models in Sect. 7 and to atmospheric models in Sect. 8. We then put limits on the masses of lower-mass companions in Sect. 9, and finally the predictions of evolutionary and atmospheric models and previous determinations are compared in Sect. 10.

2. Observations and reduction

ε Indi Ba, Bb were observed with the ESO VLT using FORS2/UT1 (Appenzeller et al. 1998) for optical photometry and spectroscopy, ISAAC/UT1 (Moorwood et al. 1998) for near-to thermal-IR photometry and spectroscopy, and NACO/UT4 (Lenzen et al. 2003; Rousset et al. 2003) for deep near-IR AO imaging. In all observations except those using NACO, the point-spread functions (PSFs) of the two sources were partially blended, even under excellent observing conditions with seeing always less than $0.7''$.

2.1. Optical photometry

Broadband $VRIz$ photometry was obtained on June 19 and July 20 2004 (UT) using FORS2 (2 CCDs each 2048×4096 pixels) in high resolution mode with 2×2 binning resulting in a plate-scale of $0.125'' \text{ pixel}^{-1}$ and a field-of-view of $4.25' \times 4.25'$. ε Indi Ba and Bb were separated by $\sim 0.84''$ under photometric conditions with median seeing of $0.55'' \text{ FWHM}$. Five images dithered by $1'$ from a central position were obtained in each filter except the R -band where twelve dithered images were taken. Individual exposure times were 500 s, 60 s, 20 s, and 10 s in the $VRIz$ bands, respectively, giving total integration times of 42 min, 12 min, 100 s, and 50 s. Sky subtraction and flat-fielding were carried out with standard IRAF programs. As seen in Fig. 1, both components of the binary are well-detected in the RIZ bands, but ε Indi Bb is only marginally detected in the V -band. We used the FORS2 Bessell V , Special R , Bessell I , and Gunn z broadband filters. Observations of the standard star fields PG 2213-006 and Mark-A (Landolt 1992) were taken for photometric calibration which is discussed in detail in Appendix C.

The large field-of-view meant there were sufficient bright field stars with which to model the PSF and so DAOPHOT/IRAF PSF-fitting was employed to extract the individual fluxes of the two brown dwarfs. For the RIZ bands, each of the images were fit separately to allow a determination of the accuracy of the profile fitting which is included in the uncertainties of the derived magnitudes. In the V -band, ε Indi Bb was only marginally detected, so we were unable to fit PSFs to the two components of the binary. To extract the photometry of both sources, we used a small aperture to measure the flux of the brighter source ensuring there was no appreciable contaminant flux from the fainter source. We then extracted the photometry of the combined source with a larger, circular aperture and, using the curve of growth of brighter stars in the field, derived the excess flux due to ε Indi Bb and thus an upper limit on the V -band flux.

The measured flux ratio and the central wavelength and width for each of the observed filters is listed in Table 1, while Table 2 lists the derived photometry.

2.2. Near- and thermal-IR photometry

The ISAAC imager was used on November 5 and 11 2003 (UT) to obtain photometry of ε Indi Ba, Bb in the ISAAC JHK_SLM_{NB} filters. ISAAC was used with the ALADDIN array (1024×1024 pixels) in long-wavelength imaging modes

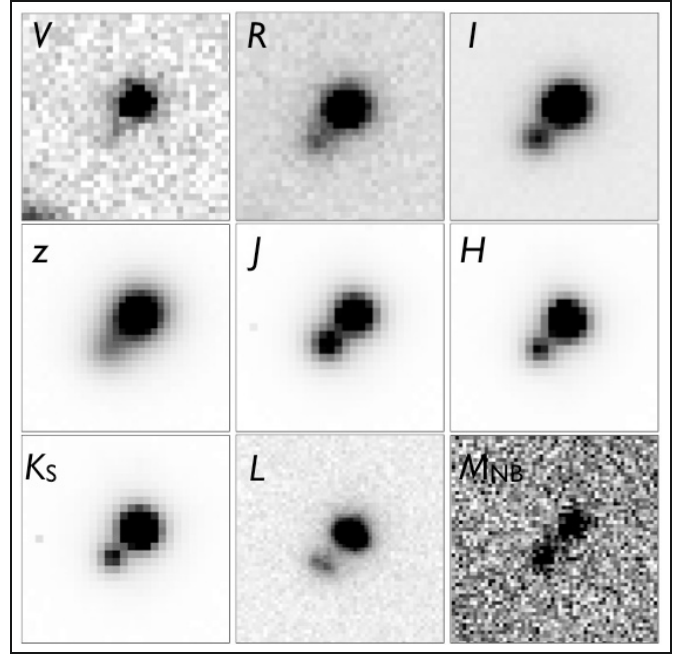


Fig. 1. From left to right and top to bottom, FORS2 $VRIz$ and ISAAC JHK_SLM_{NB} images of ε Indi Ba, Bb. Each image is a $4'' \times 4''$ subsection of the full image. North is up, East left. The object to the south-east of the V -band image is a faint galaxy not seen in the other pass-bands. The L -band profiles are seen to be slightly elliptical. The V and M_{NB} -band images are the stacked images of all observations in those pass-bands.

Table 1. The flux ratio (Ba/Bb) of ε Indi Ba, Bb in the observed FORS2 and ISAAC filters and the effective wavelength and half-power width of those filters.

Observed passband	Ratio (Ba/Bb)	λ_{eff} (μm)	$\Delta\lambda$ (μm)
V	9.82 ± 0.66	0.554	0.112
R	4.81 ± 0.07	0.655	0.165
I	5.04 ± 0.05	0.768	0.138
z	3.85 ± 0.03	0.910	0.131
J	2.28 ± 0.02	1.25	0.29
H	5.27 ± 0.06	1.65	0.30
K_S	7.12 ± 0.02	2.16	0.27
L	4.50 ± 0.16	3.78	0.58
M_{NB}	1.35 ± 0.15	4.66	0.10

See Appendix C for a description of photometric calibration and transformation to standard systems. All except the V -band ratio were measured using PSF-fitting (see Sect. 2.1).

LWI3 and LWI4 for the JHK_S and LM_{NB} imaging, respectively, resulting in plate-scales of $0.148'' \text{ pixel}^{-1}$ and $0.071'' \text{ pixel}^{-1}$ and fields-of-view of $151 \times 151''$ and $73 \times 73''$.

ε Indi Ba and Bb were separated by $\sim 0.77''$ at this epoch and were observed under photometric conditions with typical seeing of $\sim 0.45'' \text{ FWHM}$. The JHK_S images were taken at three positions dithered by $\sim 14''$ with total integration times of 3.5 min in each of the three filters. The three offset images were combined to remove the sky flux and then flat-fielded with standard IRAF programs. The L and M_{NB} images were taken in chop-nod mode with a throw of $\sim 20''$ and total exposure times of 2 min in the L -band, and 4 min in the M_{NB} -band. The images were flat-fielded and the half-cycle frames subtracted in the standard manner producing three sky-subtracted images at different positions on the array.

Table 2. The derived apparent magnitudes for ε Indi Ba, Bb.

Passband	Ba	Bb
<i>V</i>	24.12 ± 0.03	$\geq 26.60 \pm 0.05$
<i>R</i>	20.65 ± 0.01	22.35 ± 0.02
<i>I</i>	17.15 ± 0.02	18.91 ± 0.02
<i>z</i>	15.07 ± 0.02	16.53 ± 0.02
<i>J</i>	12.20 ± 0.03	12.96 ± 0.03
<i>H</i>	11.60 ± 0.02	13.40 ± 0.03
<i>K</i>	11.42 ± 0.02	13.64 ± 0.02
<i>L'</i>	9.71 ± 0.06	11.33 ± 0.06
<i>M'</i>	10.67 ± 0.23	11.04 ± 0.23

The optical magnitudes are in the FORS2 system as described in Appendix C, and the near-IR magnitudes have been transformed into the MKO *JHKLM'* filters via synthetic photometry. The uncertainties for both objects are dominated by the uncertainties on the measured flux ratio and the standard star magnitudes. Absolute magnitudes may be derived using the distance modulus of -2.205 .

The ISAAC field-of-view was found to be mostly empty, and most importantly with no stars bright enough to fit a model PSF. Therefore, a custom profile-fitting routine was implemented to determine the flux ratio of the partially-blended objects (see Appendix A). The total flux of the two objects was then measured by aperture photometry. The centre and size of a circular aperture were chosen so as to minimise the sky noise contribution while ensuring the total flux was not biased toward either object by including substantially more of the profile wings of one object than the other. The photometric calibration is discussed in detail in Appendix C and the derived near-IR photometry is listed in Table 2.

2.3. Photometric variability

Koen (2005) detected I_c -band variability in optical photometry of the combined ε Indi Ba, Bb system on time-scales of hours, reporting a linear rise in the I_c -band of $\sim 0.16^m$ over the course of 3.6 h. Table 3 shows the I -band magnitudes for the combined system from different studies. For comparison, our observations have been combined to give the magnitude of the unresolved system. However, a direct comparison is hindered by the different response functions employed in these measurements. We find that a shift in filter response of 100 \AA is sufficient to explain the spread in the I -band magnitudes due to the steep rise in T dwarf optical spectra, and so may shield any intrinsic variability.

Evidence for variability of ε Indi Ba, Bb of $\sim 0.05^m$ was also found by Koen et al. (2005) in the near-IR. Table 4 shows the 2MASS *JHK_S* magnitudes extracted from our flux calibrated spectra (see Appendix C) and the 2MASS magnitudes of McCaughrean et al. (2004) and Kasper et al. (2009). These mostly agree within the stated uncertainties with the exception of the H -band magnitude of ε Indi Bb. However, the photometry of McCaughrean et al. and Kasper et al. was acquired in the VLT/NACO system with an H -band filter which extends into the region of high telluric water absorption, possibly accounting for the differing results. The uncertainties on our near-IR photometry are of similar magnitude to the proposed variability.

We plan to use the near-IR photometry (*JHK_S*) obtained as part of the astrometric monitoring of this binary to further investigate any variability over the monitoring epochs (\sim monthly from August 2003 to present) to probe longer-term variability than that detected by Koen et al. (2005).

Table 3. The I -band magnitudes adopted for the combined ε Indi Ba, Bb system by different studies.

Date	ε Indi Ba, Bb	Reference
1997.771	16.59 ± 0.10	SSS-UK
1999.666	16.77 ± 0.10	SSS-UK
2000.781	16.90 ± 0.12	DENIS
2004.462	16.70 ± 0.04	Koen (2005)
2004.546	16.95 ± 0.03	This work

We have used the FORS2 Bessell I -band filter which is similar to the DENIS I -band, while Koen (2005) used the Cousins I -band.

Table 4. The 2MASS magnitudes adopted for ε Indi Ba, Bb in different studies.

Passband	Ba		
	McC04	K09	This work
2MASS <i>J</i>	12.29 ± 0.02	12.33 ± 0.02	12.29 ± 0.03
2MASS <i>H</i>	11.51 ± 0.02	11.54 ± 0.02	11.50 ± 0.03
2MASS <i>K_S</i>	11.35 ± 0.02	11.37 ± 0.02	11.38 ± 0.03
Passband	Bb		
	McC04	K09	This work
2MASS <i>J</i>	13.23 ± 0.02	13.19 ± 0.03	13.23 ± 0.03
2MASS <i>H</i>	13.27 ± 0.02	13.36 ± 0.03	13.19 ± 0.03
2MASS <i>K_S</i>	13.53 ± 0.02	13.51 ± 0.02	13.49 ± 0.03

McC04 refers to McCaughrean et al. (2004) for which we have assumed the uncertainties on the photometry to be equal to the uncertainty on the 2MASS photometry of the unresolved system. K09 is the study of Kasper et al. (2009).

2.4. AO deep companion search

NAOS/CONICA (NACO) was used on November 7 2003 (UT) to obtain deep adaptive-optics (AO) H -band imaging of the field around ε Indi Ba, Bb. The N90C10 dichroic was used to send 10% of the source flux to the science camera and 90% to the IR wavefront sensor (IR WFS). The median natural seeing conditions were $0.58''$ FWHM at the time of our observations and with the AO correction we obtained a FWHM of $0.12''$ in the final combined image.

The S27 camera was used with a plate-scale of $0.027'' \text{ pixel}^{-1}$ resulting in a field-of-view of $27.7'' \times 27.7''$. We obtained a total of 72 individual images with exposure times of 135 s, giving a total integration time of 162 min. The 9-point dither pattern used resulted in a continuous radial coverage of $10.94''$ measured from the position of ε Indi Ba, corresponding to 39.6 AU at 3.622 pc. Sky subtraction, flat-fielding, image alignment and stacking were standard.

As the two sources were well-separated, we were able to employ DAOPHOT/IRAF to fit a PSF to ε Indi Ba and use this as a model to subtract Bb, iteratively fitting the PSF and subtracting until Bb was well-removed. This image of Ba alone was then used to add scaled and offset objects into the original image to investigate our detection limits. We find no sources from 7 AU (71 pixels, $1.93''$) out to the image edge, corresponding to 39.7 AU, with flux greater than 0.1% of ε Indi Ba, corresponding to a peak pixel flux 5σ above the background, or a source H -band magnitude of 19.1^m which would have been detectable in our deep image.

Closer to ε Indi Ba, Bb, the noise increases due to the Poisson noise from the source flux and so the brightness limits on any companions are higher. The pixelation of the profile also acts to suppress the visibility of close companions. We find

no sources with a flux greater than 2% of the ε Indi Ba flux ($H = 15.8^m$) down to 0.83 AU (8.5 pixels, $0.23''$) from Ba or Bb, and down to 0.4 AU (4.3 pixels, $0.12''$) from each object, we can discount any sources with more than 10% of the ε Indi Ba flux ($H = 14.1^m$). In Sect. 9 we use these flux limits to derive the mass limits on any possible companion.

2.5. Optical spectroscopy

FORS2 (2 CCDs each with 2048×4096 pixels) was used on June 16 2004 (UT) to obtain optical ($0.63\text{--}1.07 \mu\text{m}$) spectroscopy of ε Indi Ba, Bb in long-slit mode with a $30''$ dither along the slit. We used a $0.5''$ wide slit, the HR collimator, and 2×2 binning mode, resulting in a plate-scale of $0.125'' \text{ pixel}^{-1}$. The 600RI and 600Z grisms were used to obtain the full $0.63\text{--}1.07 \mu\text{m}$ spectrum, yielding resolutions of $R \sim 1000$ at 6780 \AA and $R \sim 2000$ at 9700 \AA , while the median seeing of $0.47''$ FWHM allowed the spectra of the two objects to be resolved at this epoch when the separation was $\sim 0.84''$. Total integration times of 80 min with the 600RI grism and 38 min with the 600Z grism were obtained by co-adding 6×800 s and 5×460 s individual exposures, respectively.

The partially-blended spectra were extracted using a profile-fitting routine as described in Appendix B. Wavelength calibration used arc spectra for the 600RI grism and skylines for the 600Z grism, with excellent agreement in the crossover region. Our spectra have vacuum wavelengths. There was no visible difference between the two resolutions in the crossover region ($0.75\text{--}0.85 \mu\text{m}$), so they were combined without smoothing. Flat-fielding was carried out with lamp flats. Observations were also made of the white dwarf LTT9491 for relative flux calibration. However, these data were taken with a wider slit to the ε Indi Ba, Bb spectra and so could not be used for removal of telluric absorption. A spline was fit to the observed white dwarf spectrum which was used along with the known spectrum of LTT9491 (Oke 1990; Hamuy et al. 1994) to model the wavelength dependence of the flat-field and detector response and so remove this from our observed target spectra.

We scaled the NSO Kitt Peak atmospheric transmission spectrum of Hinkle et al. (2003) to construct a grid of atmospheric spectra with varying absorption strengths (assuming all absorbing species vary similarly with airmass) to model the atmosphere above Paranal at the time of our observations. These were Gaussian smoothed to the resolution of our observed spectra and the atmospheric model scaled to maximise removal of known features. The telluric features appear to be fully removed in the sections of the spectrum where we expect few features intrinsic to T dwarfs, which leads us to believe that we have acceptable telluric removal even across the $9300\text{--}9800 \text{ \AA}$ region where there are blended telluric and intrinsic features.

The final optical spectra have a peak signal-to-noise per pixel of ~ 300 and ~ 200 for ε Indi Ba and Bb, respectively, falling to ~ 35 and ~ 20 at 7000 \AA . The $0.6\text{--}5.1 \mu\text{m}$ spectra of ε Indi Ba, and Bb are shown in Figs. 3 and 4 in both linear and logarithmic units, and the full resolution spectra are shown in Figs. 5–7.

2.6. Near-IR spectroscopy

ISAAC and its HAWAII array (1024×1024 pixels) with a plate-scale of $0.146'' \text{ pixel}^{-1}$ was used on November 8 2003 (UT) in short-wavelength medium-resolution (SWS1-MR) mode to obtain near-IR spectroscopy from $0.9\text{--}2.5 \mu\text{m}$ of ε Indi Ba, Bb with a resolution of $R \sim 5000$. By turning the instrument

rotator, both sources (at a separation of $\sim 0.77''$ at this epoch) were simultaneously placed on the $0.6''$ wide slit with median seeing of $0.50''$ FWHM. Three 60 s exposures dithered by $20''$ along the $120''$ long slit were taken in each of twenty-one wavelength regions to cover the entire $0.9\text{--}2.5 \mu\text{m}$ range. We observed three spectral regions in the $0.98\text{--}1.10 \mu\text{m}$ domain each $0.046 \mu\text{m}$ wide, and six spectral regions in each of the $1.10\text{--}1.40 \mu\text{m}$, $1.40\text{--}1.82 \mu\text{m}$, and $1.82\text{--}2.50 \mu\text{m}$ spectral domains each covering a range of $0.059 \mu\text{m}$, $0.079 \mu\text{m}$, and $0.122 \mu\text{m}$, respectively, with a minimum cross-over between regions of $0.004 \mu\text{m}$ allowing full $0.9\text{--}2.5 \mu\text{m}$ spectra to be compiled with no gaps in coverage.

Observations were also made of the nearby G2 dwarf HD 209552 in each of the wavelength regions interspersed with the target observations in order to flux calibrate and correct for telluric absorption as first described by Maiolino et al. (1996). The airmass difference between the observations of ε Indi Ba, Bb and the telluric standard were in the range $0.07\text{--}0.17$. Tungsten-illuminated spectral flats were taken in the same configuration at the end of the night and wavelength calibration was achieved through use of OH skylines for all but four of the wavelength regions which had too few (known) skylines for a reasonable fit. In these cases, XeAr arc spectra were used and cross-over regions ensured a good match throughout.

For each of the wavelength regions, the three dithered spectral images were combined to subtract the sky background. This process leaves residuals of the order of a few percent of the observed counts in the spectrum caused by temporal variations in the strength of the sky emission, negligible for all but the strongest sky lines. The residual sky was further subtracted by taking apertures above and below the spectra and subtracting the sigma-clipped mean sky level. The images were then divided by the spectral dome flats. The partially-blended spectra were extracted in the same manner as the optical (see Appendix B). The extracted spectra of ε Indi Ba and Bb were divided by the standard star spectrum and corrected using the solar spectrum of Wallace et al. (1996) smoothed to the resolution of our observations to remove the wavelength dependence of the detector and the flat-field. In the regions of very high telluric absorption between the J and H and H and K bands where there were gaps in the observed solar spectrum ($13\,517\text{--}14\,032 \text{ \AA}$ and $18\,024\text{--}19\,317 \text{ \AA}$), we substituted the Kurucz IRRADIANCE model² (Kurucz 2005) to avoid any breaks in the coverage of our spectrum. These regions are generally omitted from published spectra, but since we have high-enough signal-to-noise and spectral resolution, we retain them to allow a comparison of the continuum flux in these regions to model predictions.

The known spectral type of the standard star, response of the filter systems used, and magnitudes of the standard stars allowed us to flux calibrate a template spectrum for each standard star in each of the $JHKL'M'$ passbands. We then employed the ratio of the observed fluxes of the targets and standard stars in the ISAAC system, and the known filter responses to flux calibrate our observed ε Indi Ba and Bb spectra. This was done separately for each passband as each region is bounded by high telluric absorption, but the optical spectra were flux calibrated by scaling to match the J -band spectrum in the $9782\text{--}9999 \text{ \AA}$ cross-over region. Figure 2 shows a comparison of our final near-IR spectra for both brown dwarfs with those from Kasper et al. (2009). No scaling has been applied to these spectra which, nonetheless, have similar absolute flux calibrations. While there are some

² <http://kurucz.harvard.edu/sun/irradiance/solarirr.tab>

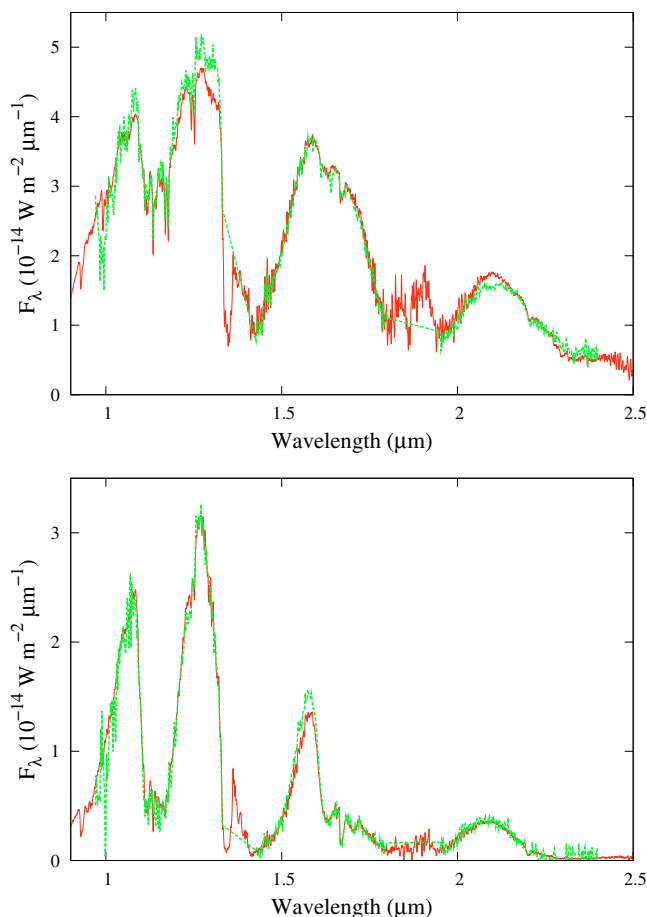


Fig. 2. Our spectra of ϵ Indi Ba and Bb (red lines), smoothed to a resolution of 17 \AA FWHM and median filtered in the regions of high telluric absorption, compared to the lower resolution spectroscopy of Kasper et al. (2009) (green lines). It is seen that the overall match of the absolute scale is reasonable. Here we have absolutely flux-calibrated using our ISAAC photometric observations, while Kasper et al. (2009) use the 2MASS point source catalogue magnitudes.

small discrepancies between the spectra, the overall match suggests that no large systematic error has been introduced by the combination of many short wavelength regions to produce our full near-IR spectrum. The final spectra have a signal-to-noise of $\sim 80/60$ (Ba/Bb) per pixel at the *J*-band peak, $100/70$ at the *H*-band peak, and $\sim 100/50$ at the peak of the *K*-band spectrum. The full resolution observed spectra of both objects are available at CDS and on the author's web-pages³.

2.7. Thermal-IR spectroscopy

ISAAC and its ALADDIN array (1024×1024 pixels) with a plate-scale of $0.146'' \text{ pixel}^{-1}$ was used on November 6–7 2003 (UT) in long-wavelength, low-resolution (LWS3-LR) mode to obtain $R \sim 600$ and $R \sim 500$ spectroscopy of ϵ Indi Ba, Bb in the spectral ranges $2.86\text{--}4.19 \text{ \mu m}$ (*L*-band) and $4.53\text{--}5.08 \text{ \mu m}$ (*M*-band), respectively, using slit widths of $0.6''$ and $1.0''$. The *M*-band spectra had to be binned before they could be extracted giving a final resolution of $R \sim 220$ at 4.75 \mu m . Both sources were placed on the $120''$ long slit and chop-nod mode was used resulting in a total on-source time of 30 min and 35 min for the *L*- and *M*-bands, respectively, with median seeing of $0.54''$ FWHM.

³ <http://www.astro.ex.ac.uk/people/rob>

The half-cycle frames were subtracted in the standard manner producing three sky-subtracted spectra at different positions on the array. Observations were also made of the solar-type star HD 210272 in the same manner to allow flux calibration and correction for telluric absorption as for the $0.9\text{--}2.5 \text{ \mu m}$ spectra. The Wallace et al. (1996) solar spectrum was incomplete with a gap in the range $4.17\text{--}4.55 \text{ \mu m}$ which affected the last $\sim 0.02 \text{ \mu m}$ of the *L*-band spectrum and the first $\sim 0.02 \text{ \mu m}$ of the *M*-band spectrum. Again, the gap was filled by the Kurucz IRRADIANCE model. Tungsten flats were taken with the same slits at the end of the night and wavelength calibration was achieved through use of XeAr arc spectra. Appendix B explains in detail how the partially-blended spectra were extracted. The final spectra have a peak signal-to-noise of $\sim 40/15$ (Ba/Bb) per pixel in the *L*-band and ~ 10 per pixel for both objects in the *M*-band.

3. Spectral classification

3.1. Near-IR spectral classification

McCaughrean et al. (2004) used the Geballe et al. (2002) and Burgasser et al. (2002) classification indices to provide spectral classifications for ϵ Indi Ba, Bb based on their *H*-band spectra. They arrived at spectral types of T1 and T6 for Ba and Bb, respectively, by employing both of the Burgasser et al. (2002) *H*-band indices and the CH_4 index of Geballe et al. (2002). The H_2O index of Geballe et al. indicated T0 and T4 and was excluded based on previous spurious spectral classification of Gl 229 B.

Given the greatly improved data here, we employ both methods of near-IR spectral index classification of Burgasser et al. (2006b), namely direct comparison of spectral indices with standard indices and against index ranges defined for each subtype. In addition, we plot our ϵ Indi Ba, Bb spectra alongside the spectra of the defined standards to allow direct morphological comparison.

Since the precise value of spectral indices is dependent on the spectral resolution, we calculate the indices with our spectra smoothed to resolutions of $R = 150$ and $R = 500$ equivalent to the resolutions for the standard stars as observed with IRTF/SPEX (at $R \sim 150$) and UKIRT/CGS4 (at $R \sim 500$). Table 5 shows the five spectral indices measured from the different resolution spectra for both ϵ Indi Ba and Bb. We also list the values for the unsmoothed spectra to quantify the effect of comparing indices for spectra at different resolutions. Spectral types inferred from each index are shown in parentheses. The range of index values for each subtype of the T class (method 2 of Burgasser et al. 2006b) has only been defined for the $R \sim 500$ CGS4 spectra of the spectral standard stars.

Figure 8 shows the spectrum of ϵ Indi Ba smoothed to $R = 150$ to match the resolution of the spectra of the standards and normalised within each of the *JHK* spectral regions, omitting the low signal-to-noise H_2O absorption regions between the bands. The spectrum is plotted along with the spectra of the T0, T1, and T2 dwarf standards observed with IRTF/SPEX (Looper et al. 2007; Burgasser et al. 2004). The T1 standard provides the best overall match, however there are some obvious discrepancies. The *J*-band spectra are normalised to one at 1.27 \mu m and although the T1 standard fits this peak and the 1.15 \mu m $\text{CH}_4/\text{H}_2\text{O}$ absorption band well, the relative strength of the 1.1 \mu m peak is not well-matched. The *H*-band is again best matched by the T1 standard with however some deficit in the flux of ϵ Indi Ba in the $1.62\text{--}1.74 \text{ \mu m}$ region which seems to indicate slightly differing levels of CH_4 absorption. The *K*-band is

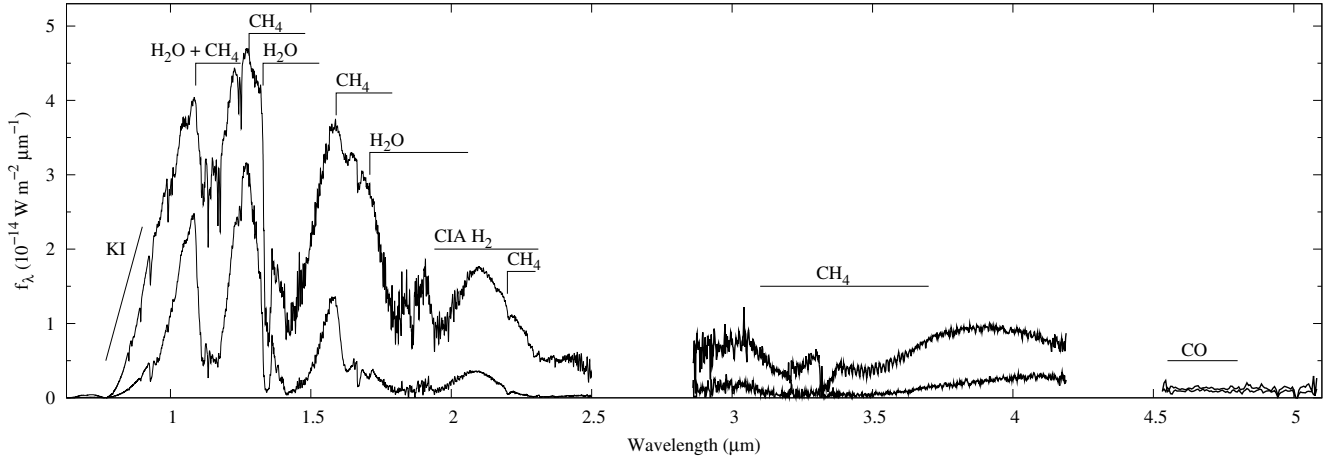


Fig. 3. Full 0.6–5.1 μm spectrum of ϵ Indi Ba and Bb (upper and lower lines respectively). Here the full resolution optical and near-IR spectra have been smoothed to 17 \AA FWHM to allow inspection of the broad features without being dominated by the many fine features seen in the full resolution spectra (see Figs. 5–7).

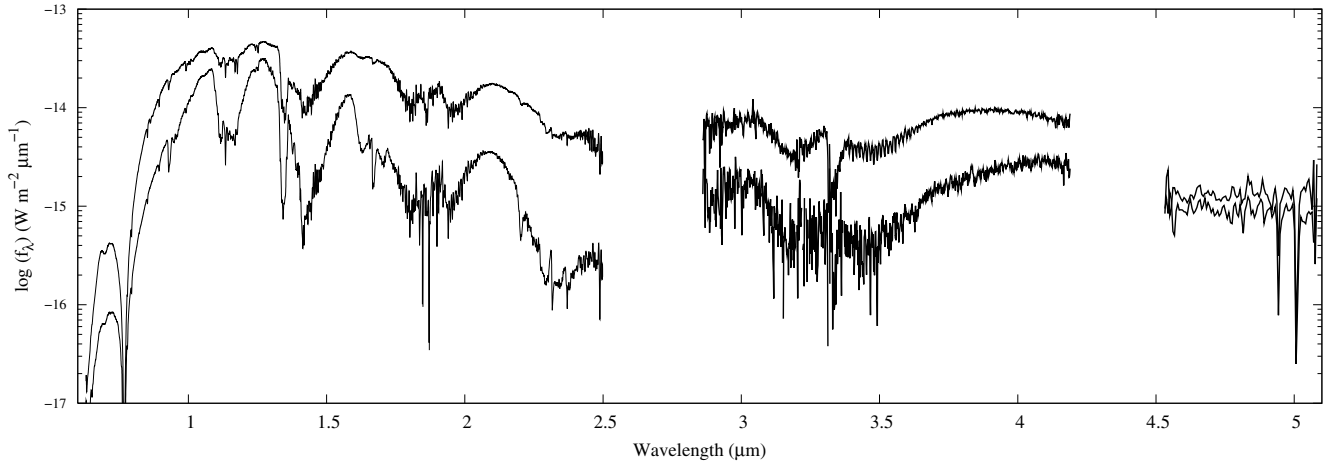


Fig. 4. The same as Fig. 3 but with the flux on a logarithmic scale.

better fit by the T2 standard, however all three standard spectra struggle to match the region beyond 2.3 μm .

Similarly, Fig. 9 shows the smoothed spectrum of ϵ Indi Bb along with the spectra of the T5, T6, and T7 dwarf standards observed with IRTF/SPEX (Burgasser et al. 2004, 2006a). The T6 standard provides the best overall match, however there are again some obvious discrepancies. The J -band spectra are normalised at 1.27 μm and although the T6 standard fits this peak and the $\text{CH}_4/\text{H}_2\text{O}$ absorption band well, the relative strength of the 1.1 μm peak is better matched by the T5 standard (although the absorption dip then no longer matches). The H -band is very well-matched by the T6 standard, with the T5 and T7 standards, respectively, over- and under-estimating the flux in the 1.62–1.74 μm region. The K -band is also best fit by the T6 standard, although again all three standard spectra differ slightly beyond 2.3 μm .

The discrepancies between the relative strength of the 1.1 μm and 1.25 μm peaks between ϵ Indi Ba, Bb and the spectral standards shown in the left-most panels of Figs. 8 and 9 could possibly be explained by the effects of different metallicities, surface gravities, or cloud cover. This may further explain the apparent excess flux in ϵ Indi Ba beyond 2.1 μm relative to the T1 standard. We discuss the effects of surface gravity and slightly sub-solar metallicity of model spectra in Sect. 8.2.

Finally, the derived near-IR spectral types for both objects from each of the three methods are summarised in Table 5. We adopt final near-IR spectral types of T1–T1.5 and T6 for ϵ Indi Ba and Bb, respectively. The uncertainty on the spectral type of ϵ Indi Ba is not due to poor signal-to-noise in our data nor the spectra of the standards, but rather is presumably due to second order spectral variations due to differences in metallicity and surface gravity.

3.2. Optical spectral classification

We have also derived spectral types from our optical spectra based on the optical T dwarf classification scheme of Burgasser et al. (2003). The spectral indices are all defined for wavelengths above 0.90 μm and so only use the higher signal-to-noise portion of the standard star spectra. Table 6 shows the value of the four indices calculated from our full resolution spectra, along with the derived mean spectral type and the classification from direct comparison to the spectral standards defined by Burgasser et al. We do not smooth the spectra for this comparison. The direct spectral comparison is shown in Figs. 10 and 11.

The optical classification broadly agrees with the near-IR classification for these two T dwarfs with spectral types of T0–T2 for ϵ Indi Ba and T6.0–T6.5 for ϵ Indi Bb. It is clear that

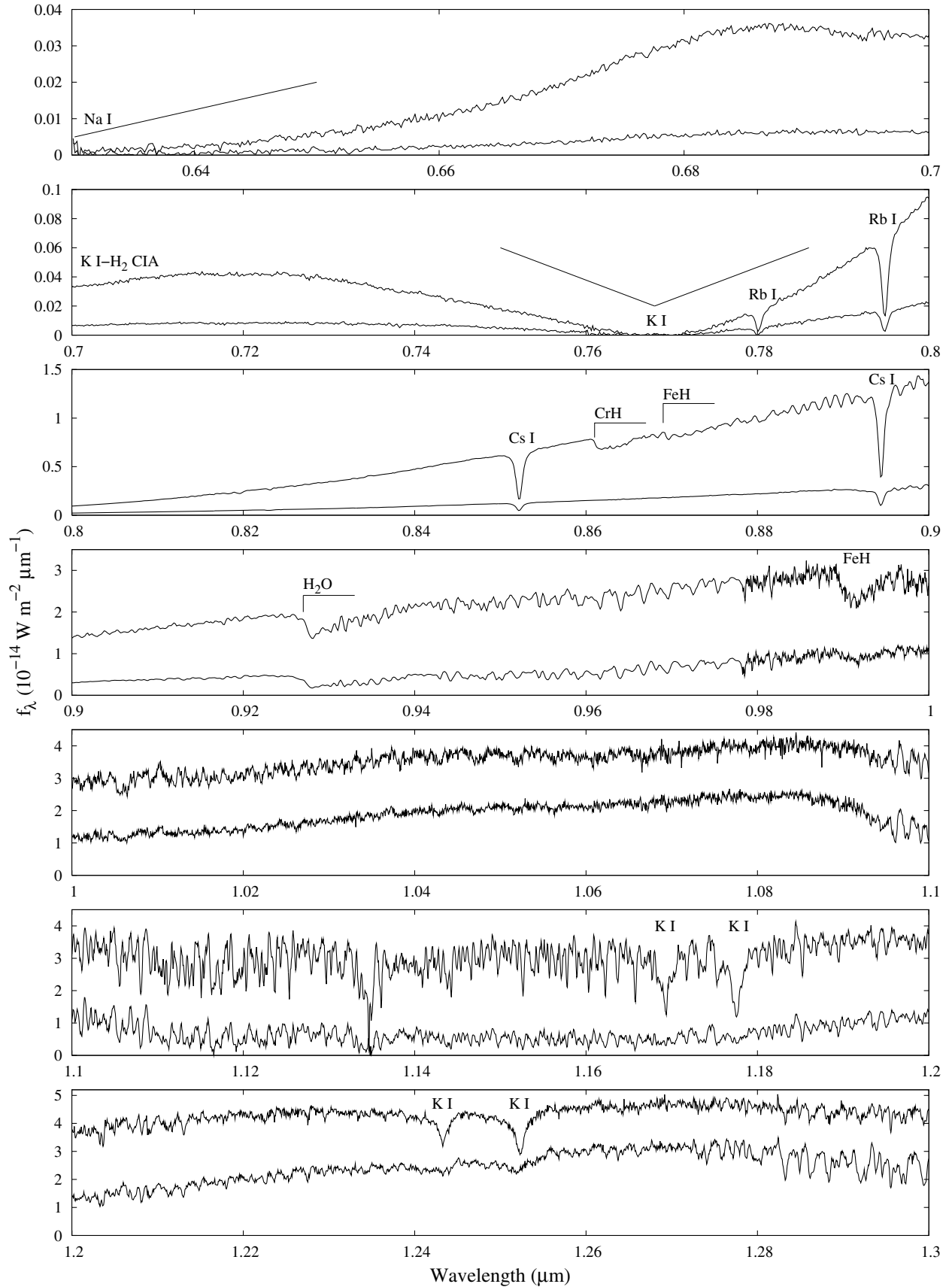


Fig. 5. The full resolution spectra of ϵ Indi Ba (top line) and Bb for 0.63–1.3 μm . The FORS2 optical data is joined to the higher-resolution ISAAC near-IR data at 0.978 μm where we start to see even finer spectral features due to the higher spectral resolution and high signal-to-noise. Comparison of the two spectra reveals much of the apparent “noise” to be real spectral features present in both objects. The resolution is 6.8 \AA FWHM up to $\lambda = 0.79 \mu\text{m}$, 6.5 \AA FWHM for $\lambda = 0.79\text{--}0.978 \mu\text{m}$, 1.8 \AA FWHM for $\lambda = 0.978\text{--}1.1 \mu\text{m}$, and 2.4 \AA FWHM for $\lambda = 1.1\text{--}1.3 \mu\text{m}$. Key spectral features are labelled. See McLean et al. (2003) for a detailed discussion of features identified in brown dwarf spectra.

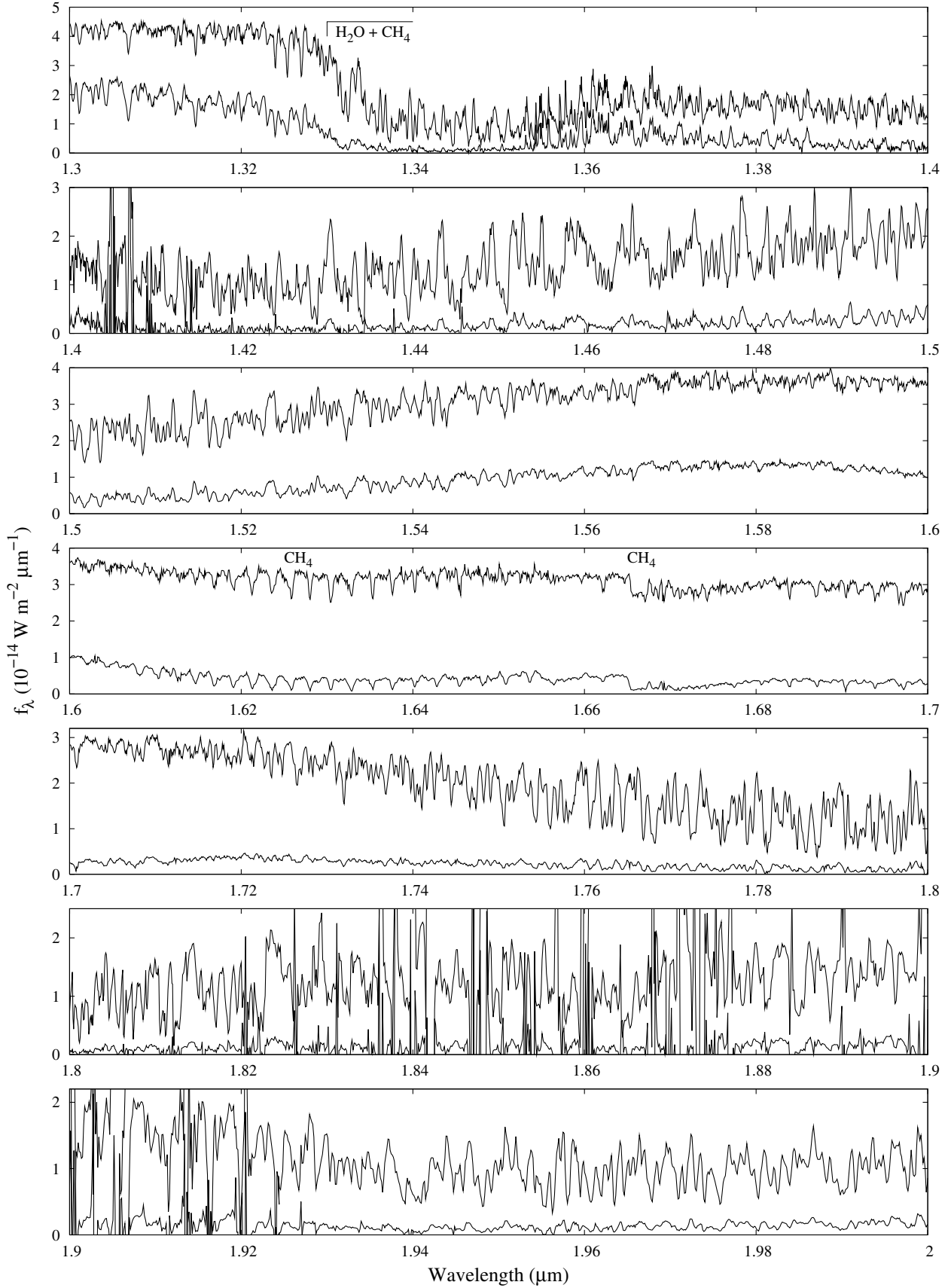


Fig. 6. Same as Fig. 5 but resolution is 2.4 \AA FWHM for $\lambda = 1.3\text{--}1.4 \mu\text{m}$, 3.2 \AA FWHM for $\lambda = 1.4\text{--}1.82 \mu\text{m}$, and 4.9 \AA FWHM for $\lambda = 1.82\text{--}2.0 \mu\text{m}$. The regions $1.40\text{--}1.41 \mu\text{m}$ and $1.82\text{--}1.92 \mu\text{m}$ have many artefacts due to high levels of telluric contamination. However, the high signal-to-noise and spectral resolution of these data allow us to extract the object spectra between the water lines, and so even in these regions we have a measure of the continuum flux.

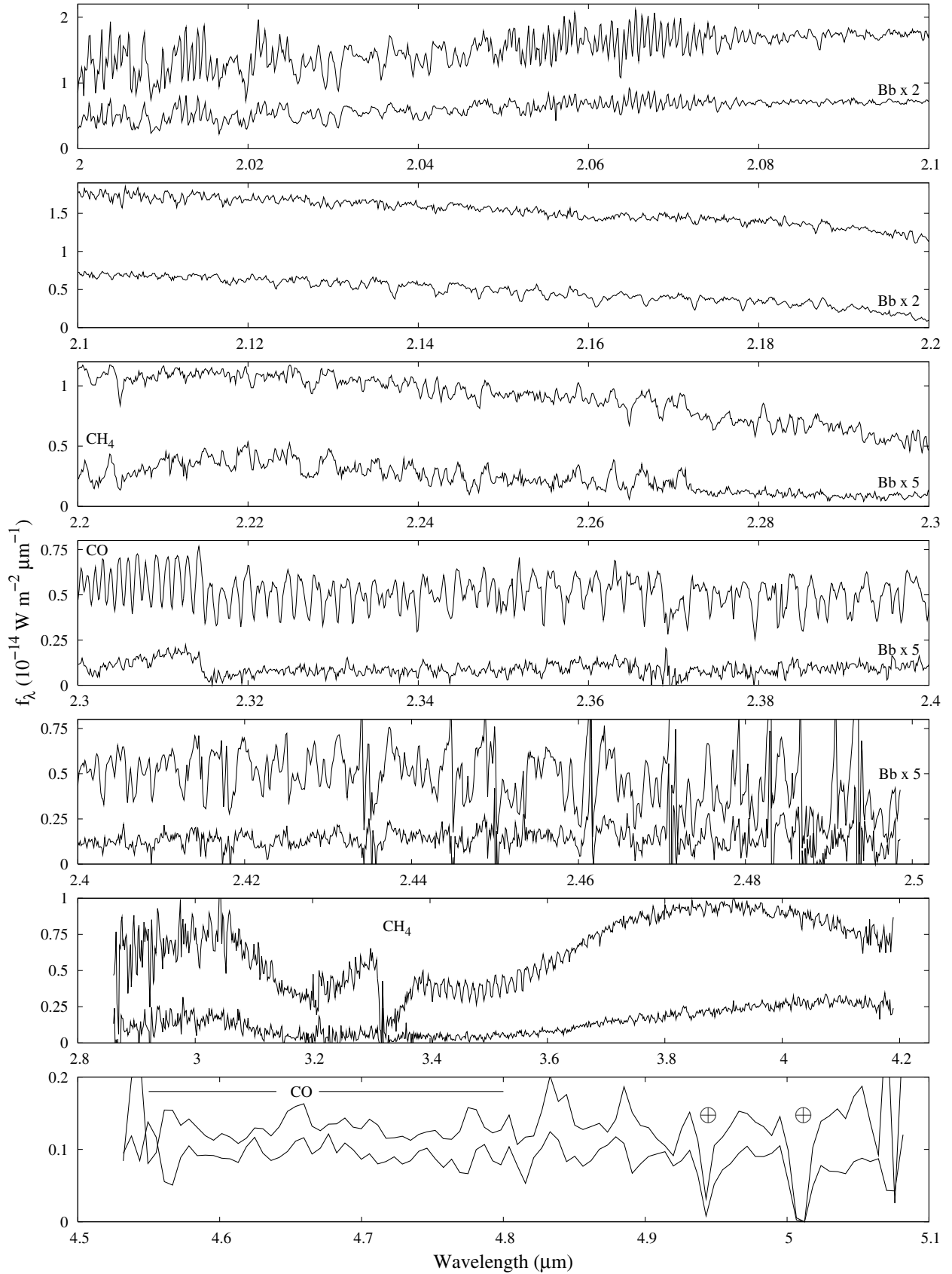


Fig. 7. Same as Fig. 5 but the observed spectra have gaps 2.50–2.86 μm and 4.19–4.53 μm between the near-IR and the *L*- and *M*-bands. The resolution is 4.9 \AA *FWHM* for $\lambda = 2.0\text{--}2.5 \mu\text{m}$, 60 \AA *FWHM* for $\lambda = 2.86\text{--}4.19 \mu\text{m}$, and 216 \AA *FWHM* for $\lambda = 4.5\text{--}5.1 \mu\text{m}$. For clarity, the flux of ϵ Indi Bb has been increased by a factor of 2 in the range 2.0–2.2 μm and by a factor 5 in the range 2.2–2.5 μm . The telluric features in the *M'*-band (marked with \oplus) are due to very bright sky emission which dominates the source signal. The artefacts seen in the region 2.43–2.50 μm are again due to high levels of telluric contamination.

Table 5. Spectral indices and classifications for ε Indi Ba, Bb.

Source	H ₂ O–J	CH ₄ –J	H ₂ O–H	CH ₄ –H	CH ₄ –K	Direct	M1	M2
Spectra smoothed to $R = 150$								
ε Indi Ba	0.650 (T0.0)	0.656 (T0.0)	0.592 (T0.0)	0.873 (T2.0)	0.587 (T2.0)	T1.0	T1.0	...
ε Indi Bb	0.172 (T6.0)	0.305 (T6.5)	0.308 (T5.5)	0.295 (T6.0)	0.178 (T5.5)	T6.0	T6.0	...
Spectra smoothed to $R = 500$								
ε Indi Ba	0.652 (.../...)	0.657 (T1.0/T1.5)	0.589 (T1.0/T0.5)	0.872 (T2.0/T2.0)	0.588 (T2.0/T2.0)	T1.0	T1.5	T1.5
ε Indi Bb	0.171 (T6.0/T6.0)	0.302 (T6.0/T6.0)	0.303 (T6.0/T6.0)	0.290 (T6.0/T6.0)	0.180 (T5.5/T5.5)	T6.0	T6.0	T6.0
Unsmoothed spectra								
ε Indi Ba	0.645	0.660	0.589	0.870	0.589	T1.0
ε Indi Bb	0.171	0.307	0.299	0.287	0.178	T6.0

The spectra have been smoothed to two resolutions to emulate the observations of the spectral standard stars defined by [Burgasser et al. \(2006b\)](#). The indices derived from our unsmoothed data have been included to quantify the uncertainty when measuring indices from spectra at different resolutions. M1 refers to method 1 of [Burgasser et al.](#) where the measured spectral indices are compared to that of each of the standard stars, and M2 refers to their method 2 where the measured spectral indices are compared to a range of values for each spectral type. Direct classification compares the overall spectral shape to the standard star spectra. The spectral type derived from each index is shown in parentheses after each measurement with only M1 being defined for a resolution of $R = 500$. The average spectral type from each method is shown on the right-hand side. Only direct classification is possible for our unsmoothed spectra. The range of the H₂O–J index is ill-defined for the earliest T dwarfs and is therefore omitted for ε Indi Ba.

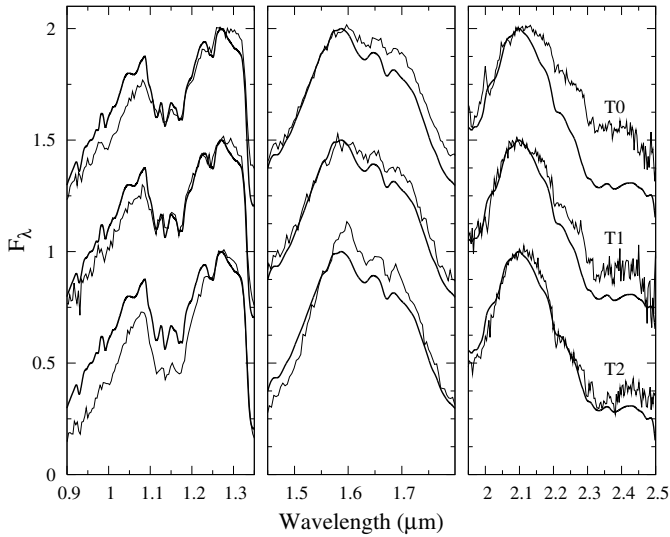


Fig. 8. Smoothed spectrum (30 \AA FWHM) of ε Indi Ba (thick lines) and spectra of the T0 (SDSS 120747.17+024424.8; [Looper et al. 2007](#)), T1 (alternate standard SDSS 015141.69+124429.6; [Burgasser et al. 2004](#)), and T2 (SDSS J125453.90-012247.4; [Burgasser et al. 2004](#)) spectral standards. The three panels show the *JHK* bands omitting the lower signal-to-noise H₂O absorption regions between the bands. Spectra are normalised to unity at $1.27 \mu\text{m}$ in the *J*-band, at $1.58 \mu\text{m}$ in the *H*-band, and at $2.10 \mu\text{m}$ in the *K*-band and offset to show the ε Indi Ba spectrum against each of the spectral standards.

our high signal-to-noise optical spectra will be useful as standards for future comparisons of optical T dwarf spectra.

4. Constraints from ε Indi A

The binary ε Indi Ba, Bb is a common proper motion companion to the K4.5V primary, ε Indi A, which allows us to constrain some of the fundamental properties of the ε Indi system. Most obviously, since the parallax of the primary was measured by HIPPARCOS ([Perryman & ESA 1997](#)), we have an accurately known distance. This was updated in the reanalysis of [van Leeuwen \(2007\)](#) to yield 3.6224 ± 0.0037 pc. The uncertainty on the distance to ε Indi Ba, Bb is somewhat larger: although we know the projected separation of the primary and

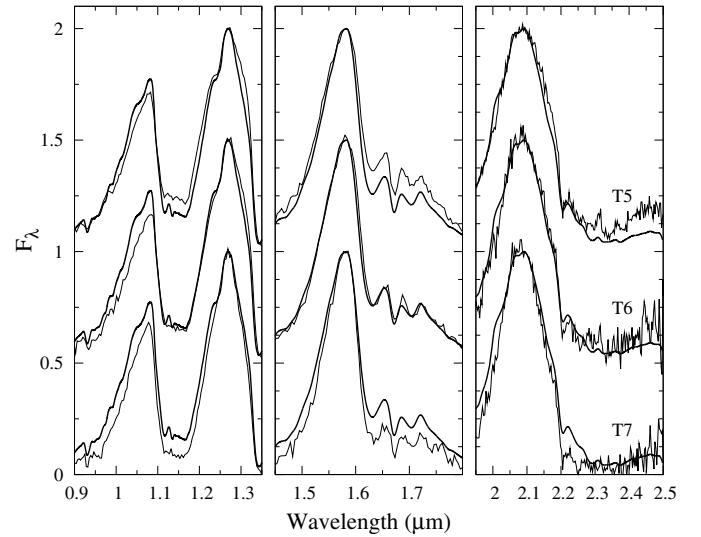


Fig. 9. Smoothed spectrum (30 \AA FWHM) of ε Indi Bb (thick lines) and spectra of the T5 (2MASS 15031961+2525196; [Burgasser et al. 2004](#)), T6 (SDSS 162414.37+002915.6; [Burgasser et al. 2006a](#)), and T7 (2MASS 0727182+171001; [Burgasser et al. 2006a](#)) spectral standards. Plotted regions and normalisation are as in Fig. 8.

brown dwarf binary to be 0.007 pc, we do not know the line-of-sight separation. This added uncertainty should be resolved by the ongoing absolute astrometric monitoring which along with the mass ratio of the ε Indi Ba, Bb system, allows determination of the parallax of the brown dwarf binary.

Similarly, determinations of the metallicity of the primary can be applied to the brown dwarf companions assuming them to be co-eval and born from the same molecular material. The metallicity of ε Indi A has been studied by a number of authors who arrive at somewhat differing results due to the chosen spectral lines and the different models with which the spectra are fit to derive the abundances. [Abia et al. \(1988\)](#) derived a metallicity of $[\text{Fe}/\text{H}] = -0.23$, while the Geneva group reported metallicities in the range $[\text{Fe}/\text{H}] = -0.2$ – $+0.06$ ([Santos et al. 2001, 2004](#)) with their most recent determination of $[\text{Fe}/\text{H}] = -0.2$ reported by [Sousa et al. \(2008\)](#). These results suggest that ε Indi A, and by association ε Indi Ba, Bb, appear to have slightly sub-solar metallicity. In Sect. 8.2 we show atmospheric models with both

Table 6. Optical spectral indices and classifications for ε Indi Ba, Bb.

Index	ε Indi Ba	ε Indi Bb
Cs I(A)	2.147 (T2.0 \pm 1.0)	1.738 (T6.0 \pm 1.0)
CrH(A) / H ₂ O	0.906 (T0.0 \pm 1.0)	0.452 (T6.0 \pm 1.0)
FeH(B)	1.237 (<T4?)	1.109 (T6.5 \pm 0.5)
Colour-e	3.323 (T0.0 \pm 1.0)	4.135 (>T2)
Mean	T0.5	T6.0
Direct	<T2.0	T6.0

The spectra have not been smoothed to derive these indices. Direct classification compares the overall spectral shape with the standard star spectra. The spectral type derived from each index is shown in parentheses after each measurement. The spectral range of the FeH(B) index is limited to types later than T2 and the range of the colour-e index to types earlier than T2. The approximate classification from direct comparison for Ba is due to the lack of a T0 or T1 optical spectral standard.

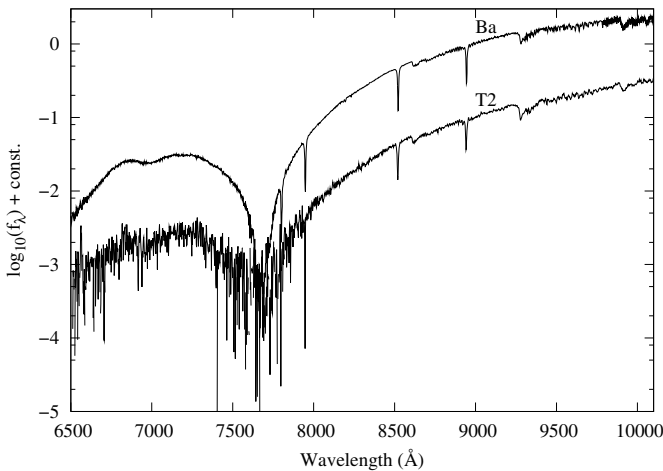


Fig. 10. Optical spectrum of ε Indi Ba and the T2 (SDSS 1254-0122, Burgasser et al. 2003) optical spectral standard. There is no object defined as either the T0 or T1 spectral standard in the optical. The ε Indi Ba spectrum is normalised to unity at 9000 Å and the T2 standard spectrum is offset by 1 dex for clarity.

[M/H] = 0.0 and -0.2 fit to our spectroscopic observations. Note however, that [M/H] refers to the global metallicity and also depends on the abundance of α -elements (cf. Ferraro et al. 1999), so is not necessarily equivalent to [Fe/H].

In previous analyses, the age estimate of 0.8–2.0 Gyr for ε Indi A from Lachaume et al. (1999) was used to make predictions from evolutionary models. Using this age range McCaughrean et al. (2004) derived model masses of 47 ± 10 and $28 \pm 7 M_{\text{Jup}}$. As we will discuss, we now have direct determinations of the luminosity of both brown dwarfs and of the system mass. However, the age of an individual system is a notoriously difficult parameter to ascertain and so we will return to discuss the reliability of this age in Sect. 7.3.

5. Luminosity determination

McCaughrean et al. (2004) used their photometry of ε Indi Ba, Bb and estimated bolometric corrections from the spectral type– M_{bol} relation of Golimowski et al. (2004) to derive luminosities of $\log L/L_{\odot} = -4.71$ and -5.35 for ε Indi Ba and Bb, respectively, with estimated uncertainties of $\pm 20\%$. Here we use our flux calibrated spectra to derive luminosities directly following a similar process to Golimowski et al. (2004).

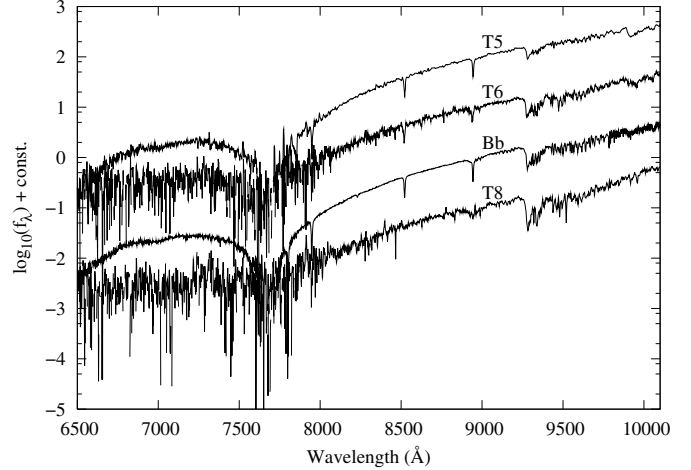


Fig. 11. Optical spectrum of ε Indi Bb and the T5 (2MASS 0559-1404; Burgasser et al. 2003), T6 (SDSS 1624+0029; Burgasser et al. 2000), and T8 (2MASS 0415-0935; Burgasser et al. 2003) optical spectral standards. There is no object defined as the T7 spectral standard in the optical. Spectra are normalised at 9000 Å and offset in steps of 1 dex for clarity.

We sum the 0.63–5.1 μm flux with linear interpolation in the unobserved regions 2.5–2.86 μm and 4.19–4.53 μm . This is extended to the mid-IR using the *Spitzer* Infrared Spectrograph (IRS, Roellig et al. 1998) 5–15 μm (Roellig et al. 2004) and 10–19 μm spectra (Mainzer et al. 2007) of the unresolved ε Indi Ba, Bb system. To approximate the mid-IR spectrum of each object and to ensure an accurate representation of the absolute fluxes, we also used the resolved mid-IR VLT/VISIR photometry of Sterzik et al. (2005). These two determinations of the absolute flux of the combined system differ significantly. We found that the VISIR photometry would have to be scaled upward by $\sim 50\%$ to be fully consistent with the *Spitzer* spectrum. We therefore used these two measurements as the bounds on the total flux in this region and used the measured flux ratio of ~ 2.1 at 8.6 μm and 10.5 μm from Sterzik et al. (2005) to produce approximate spectra for each object for our luminosity determination.

Beyond this we used a blackbody tail with T_{eff} given by the model fit to the spectra (see Sect. 8). This however contributes only 0.5% and 0.9% to the total flux for ε Indi Ba and Bb, respectively, so the precise temperature used is unimportant. The mid-IR spectrum used to extend our spectroscopic measurements contributes $\sim 8.5\%$ and $\sim 14.5\%$ of the total flux of ε Indi Ba and Bb, respectively. We did not attempt to extend our observed spectra blueward for the luminosity derivation as our *V*-band photometry shows the flux to have dropped by 2–3 orders of magnitude relative to the *I*-band flux for both ε Indi Ba and Bb.

The resulting luminosities are $\log L/L_{\odot} = -4.699 \pm 0.017$ and -5.232 ± 0.020 for ε Indi Ba and Bb, respectively, with the uncertainties derived from our photometry, 20% uncertainty on the mid-IR fluxes, and an assumed 3% uncertainty on the absolute flux of the Vega spectrum used for flux calibration (Mountain et al. 1985; Hayes 1985), all of which dominates the distance uncertainty. The difference between our determination of the luminosity of ε Indi Bb and that of McCaughrean et al. (2004) is likely explained by the increased scatter in the spectral type – BC_K relation of Golimowski et al. (2004) at late-T spectral types.

6. Dynamical masses

Ongoing relative astrometric monitoring of the ε Indi Ba, Bb orbit since May 2004 has allowed a preliminary system mass of $121 \pm 1 M_{\text{Jup}}$ to be determined (Cardoso et al. 2009a; McCaughrean et al., in prep.). As mentioned previously, absolute astrometric monitoring is also ongoing (Cardoso et al., in prep.) which will determine the mass ratio of the system allowing a model independent determination of the individual masses of both ε Indi Ba and Bb. However, we can already provide some constraints on the individual masses of the brown dwarfs on the basis of our photometric and spectroscopic observations. Since we know these objects to be physically bound and so, in all likelihood, co-eval, ε Indi Ba must be more massive than its fainter companion. Additionally, we also know from the low temperatures required to produce T dwarf spectra that both objects must be substellar, therefore the more massive component must have a mass below the hydrogen burning minimum mass (HBMM) of $\sim 0.070 M_{\odot}$ ($73 M_{\text{Jup}}$) for a cloudy, approximately solar metallicity source (Chabrier et al. 2000; Saumon & Marley 2008).

Together then, the masses of these two brown dwarfs are constrained to be between $73 + 47 M_{\text{Jup}}$ and $60 + 60 M_{\text{Jup}}$, with the latter being unlikely due to the different luminosities of the two brown dwarfs. Therefore, the mass of ε Indi Ba must be in the range $60\text{--}73 M_{\text{Jup}}$ and ε Indi Bb in the range $47\text{--}60 M_{\text{Jup}}$, but with a sum of any pairing equal to $121 \pm 1 M_{\text{Jup}}$.

7. Evolutionary model comparisons

7.1. Photometry

In Table 2 we presented the apparent magnitudes of both components of the ε Indi Ba, Bb system in the FORS2 $VRIz$, and MKO $JHK'L'$ filters. Here we will compare the photometric predictions of the solar metallicity COND03 evolutionary models (Baraffe et al. 2003, hereafter B03) with the absolute magnitudes derived from our observations. However, before doing so, it is important to note the limitations of these models even if they represent the current state-of-the-art. Although reasonable predictions can be made for the near-IR colours of mid-late T dwarfs, the colours of early T dwarfs fall somewhere between the predictions of the COND03 and the DUSTY00 models (Chabrier et al. 2000). The COND03 evolutionary models neglect the effect of dust opacity in the radiative transfer, whereas the DUSTY00 models included dust but once formed it remained in the atmosphere. The newer BT-Settl atmosphere models account for the settling of some species from the atmosphere, so once incorporated into the evolutionary models may provide a more realistic match to observed colours across the L and T spectral classes.

Figures 12–14 show colour–magnitude diagrams (CMDs) comparing our ε Indi Ba, Bb photometry with the COND03 and DUSTY00 5 Gyr isochrones along with other T dwarf observations from the literature. The model JHK magnitudes have been transformed from the CIT system to the MKO system using the colour relations of Stephens & Leggett (2004), while the model L' magnitudes are left in the Johnson-Glass system and the I magnitudes in the Bessell system.

In Fig. 12, ε Indi Ba is seen to lie $\sim 0.5\text{--}1.0$ mag redward of the model isochrone, while ε Indi Bb is ~ 0.5 mag blueward. The position of the metal-poor ($-0.4 < [M/H] < -0.1$) T6 subdwarf, 2MASS 0937+2931 (Burgasser et al. 2003), is marked and seen to be bluer than ε Indi Bb. Schilbach et al. (2009) find that 2MASS 0937+2931 falls above an extrapolated $[M/H] = -0.5$

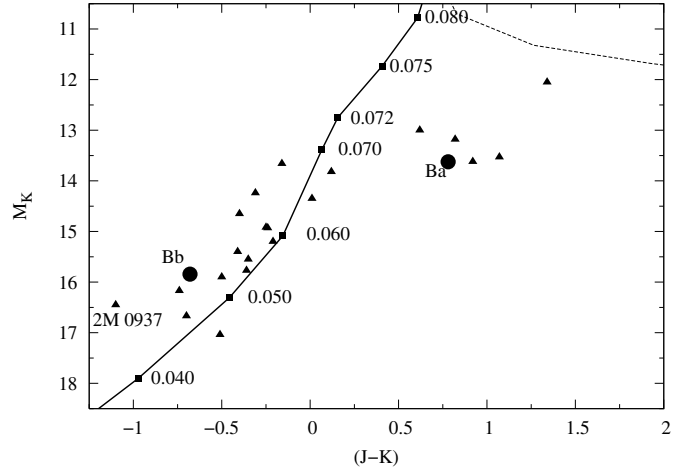


Fig. 12. $M_K - (J - K)$ colour–magnitude diagram with the 5 Gyr COND03 isochrone (Baraffe et al. 2003) with masses (in M_{\odot}) indicated as filled squares. The DUSTY00 5 Gyr isochrone (Chabrier et al. 2000) is also shown (upper, dashed line). The positions of ε Indi Ba and Bb are marked with filled circles, the filled triangles show the T dwarf observations of Knapp et al. (2004) and Chiu et al. (2006), and the metal-poor T6 subdwarf 2MASS 0937+2931 is labelled. All magnitudes are in the MKO system. We do not show isochrones for different ages as they show little variation in position, except that the same masses correspond to different magnitudes.

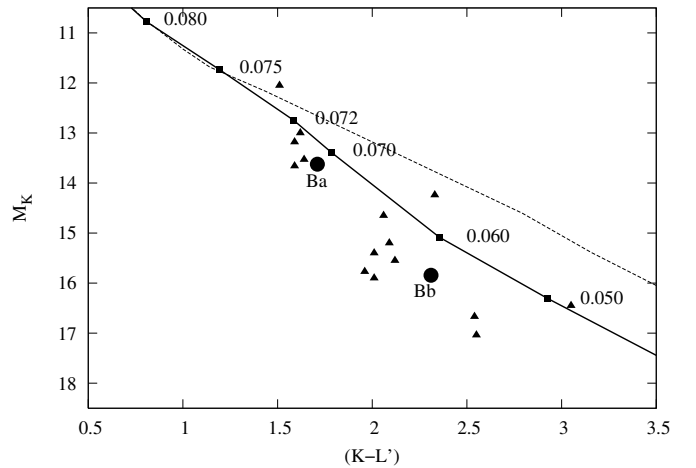


Fig. 13. $M_K - (K - L')$ colour–magnitude diagram with the 5 Gyr COND03 isochrone with masses (in M_{\odot}) indicated as filled squares. The DUSTY00 5 Gyr isochrone is also shown (upper, dashed line). Symbols are the same as in Fig. 12 with the unlabelled data from Knapp et al. (2004), Chiu et al. (2006), and Golimowski et al. (2004). The data are in the MKO system, whereas the model L' magnitude is in the Johnson-Glass system.

Baraffe et al. (1998) isochrone in an $M_K - (J - K)$ CMD and is possibly part of the thick disc or halo population. By contrast, the position of ε Indi Bb suggests only a slightly sub-solar metallicity.

Figure 13 shows that the predicted $(K - L')$ colours are a better match to our and other early T dwarf observations as the effects of clouds are much reduced in this region, but observed colours are still consistently bluer than the models implying that spectral features in these regions are not well reproduced by these models.

When optical colours are used in a CMD, the mismatch between observations and models increases. For late T dwarfs such

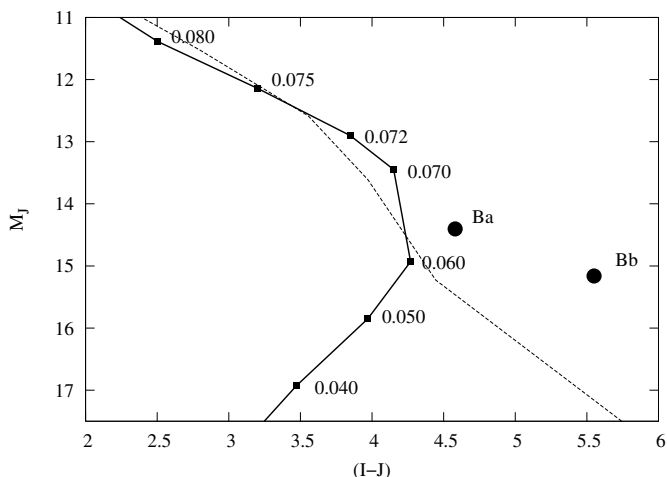


Fig. 14. $M_J - (I - J)$ colour–magnitude diagram with the 5 Gyr COND03 isochrone with masses (in M_\odot) indicated as filled squares. The DUSTY00 5 Gyr isochrone is also shown (dashed line). Symbols are the same as in Fig. 12. J -magnitudes are in the MKO system and I -magnitudes use the FORS2 Bessell I filter.

as ε Indi Bb, as shown in Fig. 14, our observed $(I - J)$ colours are significantly redder than model predictions even after accounting for differences due to the use of different filter systems. These issues will be addressed when we compare our observations with the more up-to-date atmospheric models in Sect. 8.

This discrepancy between the isochrones and the observations for the early T dwarfs is an indication of the complexity of their atmospheres where the role of clouds is greater than for later types. As brown dwarfs transition from dusty L to cloud-free mid-late T dwarfs, the observations are found to lie between the COND03 and DUSTY00 models (Baraffe et al. 2003).

7.2. Physical properties

Although the previous section has shown that neither the COND03 nor the DUSTY00 atmospheres necessarily reproduce the observed colours of T dwarfs faithfully, the comparison of properties such as luminosity, mass, and effective temperature should be more reliable as they are not so strongly dependent on the specifics of the atmospheric model used. That said, Chabrier et al. (2000) showed that the luminosity and effective temperature evolution at a specific mass are not entirely independent of the treatment of dust in the atmosphere. They find the difference between the DUSTY00 and COND03 model predictions, for a given age, can be up to 10% in effective temperature and up to 25% in luminosity with the COND03 models predicting systematically higher effective temperatures than the corresponding DUSTY00 models. With the precision of our mass and luminosity determinations, these uncertainties are significant. However, for the age and mass range of the ε Indi Ba, Bb system, the DUSTY00 evolution models predict only slightly less efficient cooling than the COND03 models, resulting in $\sim 3\%$ smaller masses, 5% larger radii and less than 3% differences in effective temperature than the COND03 models.

Additionally, Saumon & Marley (2008) have recently compared their evolutionary model predictions with the Lyon DUSTY00 and COND03 models, concluding that the differences between the corresponding cloudy and cloud-free models at intermediate ages can be explained by the lack of electron conduction in the Saumon & Marley (2008) models. The

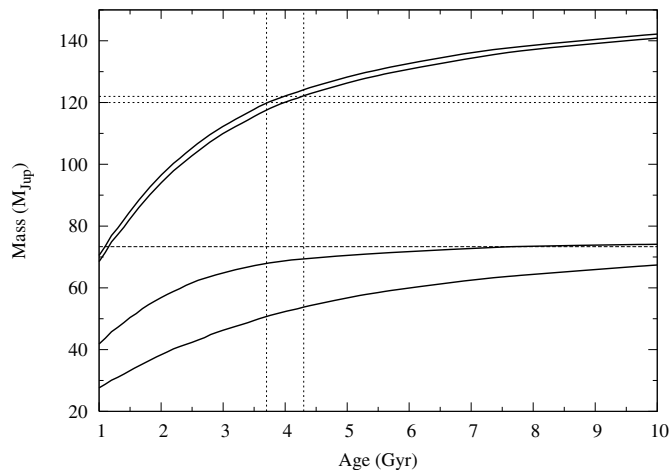


Fig. 15. Variation of mass with age for lines of constant luminosity interpolated from a fine grid of COND03 evolutionary models for the observed luminosities of ε Indi Ba and Bb (lower two curves). The upper two curves show the predicted combined mass at each age accounting for the uncertainties on the individual luminosities, while the constraints on the system mass from the dynamical monitoring are indicated by the upper two horizontal dotted lines. The lower horizontal dashed line indicates the hydrogen burning minimum mass of $0.070 M_\odot$ and the 3.7–4.3 Gyr age predicted by the COND03 models is shown by the two vertical dotted lines.

Table 7. Predictions of the parameters of ε Indi Ba and Bb from the COND03 evolutionary models.

Source	Mass (M_{Jup})	Radius (R_\odot)	T_{eff} (K)	$\log g$ (cm s^{-2})
ε Indi Ba	67.6–69.1	0.080–0.081	1352–1385	5.43–5.45
ε Indi Bb	50.0–54.5	0.082–0.083	976–1011	5.27–5.33

These parameters are derived for the age range of 3.7–4.3 Gyr given by the measured total mass (Ba+Bb) and individual luminosities.

differences seen when compared to the Burrows et al. (1997) models is found to be mainly due to the use of older non-grey atmospheres in the Burrows et al. (1997) models. We therefore employ only the Lyon models in our comparison.

Given the observed luminosities of ε Indi Ba and Bb, the evolutionary models can be used to predict the corresponding masses as a function of the system age, as shown in Fig. 15. It is immediately apparent that the original age estimate of 0.8–2.0 Gyr is inconsistent with the evolutionary models given the newly established mass of $121 \pm 1 M_{\text{Jup}}$. From the COND03 models, we find that an age range of 3.7–4.3 Gyr is necessary to accommodate the mass and luminosity constraints. Table 7 shows that for this age range, the COND03 models predict effective temperatures of 1352–1385 K and 976–1011 K for ε Indi Ba and Bb, respectively, and a mass ratio in the range 0.73–0.78. Similarly, Table 8 shows the predicted physical parameters of ε Indi Ba, and Bb for the observed luminosities and ages of 1, 5, and 10 Gyr.

7.3. Age of the ε Indi system

This age range of 3.7–4.3 Gyr for ε Indi Ba, Bb is significantly larger than the age of 0.8–2.0 Gyr estimated by Lachaume et al. (1999) for ε Indi A based on the rotational period given by Saar & Osten (1997). In fact, the measured $v \sin i$ for ε Indi A was too small to derive any meaningful rotational period and this period

Table 8. Physical parameters of ε Indi Ba, Bb derived using the observed luminosities and the COND03 models of Baraffe et al. (2003) for three ages: 1, 5, and 10 Gyr.

Source	$\log L/L_{\odot}$	Mass (M_{Jup})			Radius (R_{\odot})			T_{eff} (K)			$\log g$ (cm s^{-2})		
		1 Gyr	5 Gyr	10 Gyr	1 Gyr	5 Gyr	10 Gyr	1 Gyr	5 Gyr	10 Gyr	1 Gyr	5 Gyr	10 Gyr
ε Indi Ba	-4.699	42.0	69.8	74.1	0.093	0.080	0.079	1274	1387	1393	5.10	5.45	5.49
ε Indi Bb	-5.232	28.0	57.2	66.2	0.097	0.081	0.077	929	1019	1051	4.88	5.36	5.47

was inferred from the Ca II H&K emission observed by Henry et al. (1996), rendering it less reliable. Barnes (2007) also calculates an age of 1.03 ± 0.13 Gyr from rotation, although this uses the same inferred 22 day period. Lachaume et al. (1999) also derive an age from the Ca II H&K activity using their R'_{HK} – age relation, which suggests an age in the range 1–2.7 Gyr. However, in choosing a young age based on this activity indicator, they ignored the much greater estimate of >7.4 Gyr which they derived from the kinematic properties of the system.

Age constraints are also available if one considers the larger moving group of which ε Indi A is the eponymous member, and for which Cannon (1970) quoted an age of 5 Gyr derived from the observed ($B - V$) colour of an apparent red giant clump. However with only 15 members (Eggen 1958), it is not clear that there would be enough objects at the end of their main-sequence lives to fit this reliably. Furthermore, the moving group members given in Eggen (1958) were presumably used in Cannon (1970), although no details of the members used are given. This membership list was later revised by Eggen (1971) which excluded five stars from the original list of members. Thus, the age of this apparently elderly moving group is not a strong age constraint by itself. However λ Aurigae, another member of the moving group, has an isochronal age of 5.8 ± 0.43 Gyr from Soubiran & Girard (2005) which adds support to an intermediate age for the entire moving group, although this technique has been shown to be unreliable when applied to individual objects. This worsens toward later spectral types where the isochrones become degenerate, so isochrone fitting would be unreliable for ε Indi A, but in the case of λ Aurigae the isochrones are relatively well separated.

Finally, Rocha-Pinto et al. (2002) classifies ε Indi A as a “chromospherically young, kinematically old” star based on the disagreement between the age from activity indicators and the observed space velocities. They find a chromospheric age of 0.39 Gyr, but note that ε Indi A has no obvious Li I absorption line and so argue that it is an older star than activity suggests. The origin of these stars is as yet unknown.

After further consideration then, an age of ~ 3.7 – 4.3 Gyr for ε Indi Ba, Bb as predicted by the evolutionary models in Sect. 7.2 seems plausible at least. The discrepancy between the various age estimates highlights the problem of deriving ages for individual objects, as any one indicator cannot be entirely trusted. To address this issue, we are currently investigating the feasibility of obtaining high resolution, time-resolved spectroscopy of ε Indi A to derive an age via asteroseismology.

8. Atmospheric model comparison

The comparisons presented in Sect. 7.1 demonstrated that the COND03 and DUSTY00 models yield a relatively poor match to the observed photometric properties of ε Indi Ba and Bb. Using the newer BT-Settl atmosphere models (Allard et al. 2003; Allard, in prep.), which account both for the formation and optical effects of dust in the atmosphere and for settling

of condensates under steady-state conditions, the calculation of synthetic spectra and colours can reproduce these observations much more accurately. By allowing the description of partially settled clouds, these model atmospheres are a more appropriate comparison in particular for early T dwarfs, where the atmospheres transition from being dust-dominated to cloud-free, and so here we compare BT-Settl atmosphere models with our detailed spectral observations of ε Indi Ba and Bb.

These atmosphere models have yet to be incorporated into a self-consistent set of interior structure and evolution models, but since even the differences between the DUSTY00 and the completely cloud-free COND03 models result in only small discrepancies in cooling rates and radius evolution, our analysis should not be much compromised by applying the newer models on top of the older evolution models.

The BT-Settl models are based on version 15 of the PHOENIX stellar atmosphere code (Hauschildt & Baron 1999) with updated opacity databases, including among others the recent water line list of Barber et al. (2006) and extended methane line lists (Homeier et al. 2003). The chemical equilibrium code used in the DUSTY00 and COND03 models (Allard et al. 2001; Baraffe et al. 2003) has been modified to include grain settling effects (Allard et al. 2003). At each layer in the model atmosphere, the dust grain number densities are calculated in equilibrium to the gas phase. The timescales for condensation and growth processes and gravitational settling are then calculated following Rossow (1978) and compared to the turbulent mixing timescale to predict the median size and the fraction of grains which have settled. This fraction is then removed from the composition and a new equilibrium obtained, iterating the process until the grain density no longer changes. For more detailed results and a comparison with other cloud models see Helling et al. (2008). Turbulent mixing in the present models is calculated by interpolation from 2D and 3D radiation hydrodynamic (RHD) models with the CO5BOLD code, extending the results of Ludwig et al. (2006) to lower temperatures by including a self-consistent dust module (Freytag et al. 2010). As such, the BT-Settl models do not include any adjustable parameters, except for some freedom in the translation of the hydrodynamic velocity field in the convective overshoot region into an effective timescale. This conversion has been chosen such as to optimally reproduce the entire photometric sequence from early-L to mid-T dwarfs.

For each model spectrum of known effective temperature, we inferred a radius using our observed luminosities of ε Indi Ba and Bb, which along with the known distance, allowed us to convert the emergent flux density of the atmospheric models to the flux that would be observed from Earth. Therefore, for each model spectrum we were able to compare predicted absolute flux levels against those observed without reliance on evolutionary models. In other words, we were not free to normalise the model spectra to match our observations.

The model grid sampled effective temperature in steps of 20 K, surface gravity in steps of 0.25 dex, for solar and slightly sub-solar metallicity ($[M/H] = 0.0, -0.2$). The metal abundances

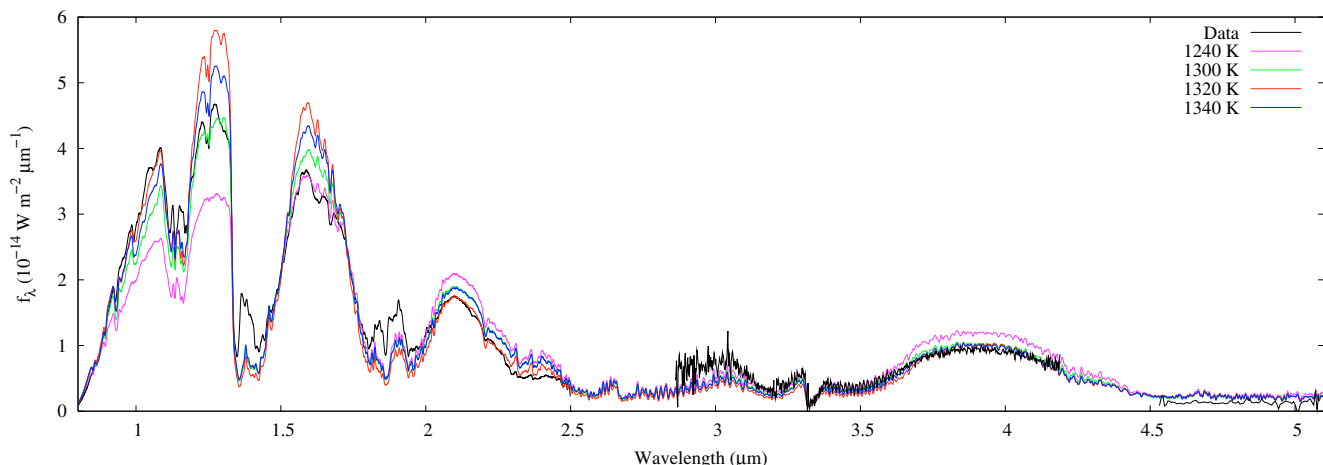


Fig. 16. Near- to thermal-IR spectrum of ϵ Indi Ba (black line) with sub-solar metallicity ($[M/H] = -0.2$) BT-Settl spectra with $T_{\text{eff}} = 1300, 1320, 1340$ K and $\log g = 5.50$ (green, red, and blue lines respectively). The $T_{\text{eff}} = 1240$ K spectrum (magenta line) is also shown to indicate the large difference between the observations and spectral models for this lower effective temperature. All spectra have been smoothed to 60 \AA FWHM and the observed spectrum median filtered to remove the lowest signal-to-noise points.

of Grevesse & Noels (1993) were employed instead of the more recent Asplund et al. (2005) abundances as the validity of the latter determination of oxygen abundance is the subject of ongoing debate given its effect on previously well-matched helioseismological theory and observations (cf. Ayres 2008; Caffau et al. 2008).

8.1. Effective temperature effects

Figure 16 shows the BT-Settl near-IR spectral models with effective temperatures in the range 1300–1340 K and $\log g = 5.50$, $[M/H] = -0.2$ compared to our spectrum of ϵ Indi Ba. Since Kasper et al. (2009) find acceptable fits to low resolution near-IR spectra of ϵ Indi Ba using models with effective temperatures of 1250 K and 1300 K, we include our 1240 K model to show the large mismatch such a low effective temperature would have with the BT-Settl models. Each of the models has an absolute flux scale set by the effective temperature and the observed luminosity of the corresponding object, therefore there is no scaling of model spectra to improve the fit to observations. We find effective temperatures in the range 1300–1340 K produce the most reasonable fit to the flux level across the spectrum and to individual features.

For higher effective temperature models, the KI lines at $1.25 \mu\text{m}$ are too strong and the FeH and CrH features around $1 \mu\text{m}$ are too deep, while by 1280 K the $1 \mu\text{m}$ features are no longer reproduced and the depth of the KI doublet is significantly reduced (see Fig. 17). Additionally, at lower temperatures, we find that the flux level of the near-IR peaks become increasingly difficult to reconcile with the observations.

Figure 18 shows the BT-Settl near-IR spectral models with effective temperatures in the range 880–960 K and $\log g = 5.25$, $[M/H] = -0.2$ compared to the data for ϵ Indi Bb. While the optical spectrum is problematic at any effective temperature (see Sect. 8.4), there is relatively little variation within this effective temperature range in the thermal-IR. Based on the near-IR alone then, we find the most reasonable fits to have effective temperatures in the range 880–940 K. Figure 18 shows that at temperatures below 900 K, the flux level of the $1.1 \mu\text{m}$ and the $2.1 \mu\text{m}$ peaks becomes progressively more depressed, and as seen in Fig. 19, at higher temperatures, the $1.25 \mu\text{m}$ KI lines are considerably deeper than observed, although the shapes of the

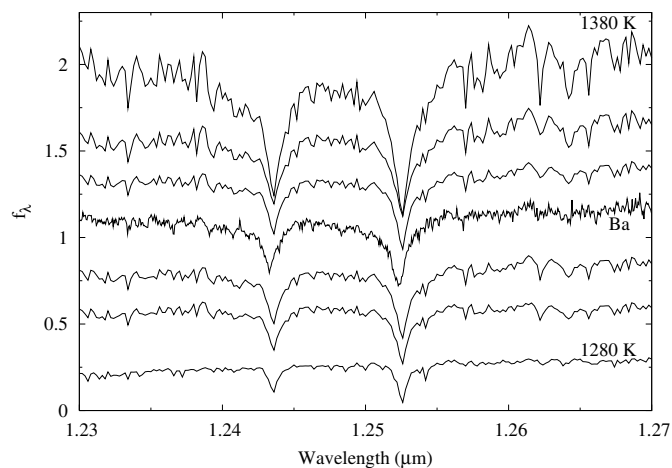


Fig. 17. $1.23\text{--}1.27 \mu\text{m}$ spectrum of ϵ Indi Ba (thicker line, fourth from top) and the $[M/H] = -0.2$, $\log g = 5.50$ BT-Settl spectra with $T_{\text{eff}} = 1280\text{--}1380$ K (increasing bottom to top in steps of 20 K). All spectra have been normalised and offset for clarity. Model spectra have been smoothed to 2.4 \AA FWHM.

tops of the $1.1 \mu\text{m}$ and $1.25 \mu\text{m}$ peaks are not well-matched by any of the models.

8.2. Metallicity and surface gravity effects

In low-mass stars, the effect of decreasing metallicity is to increase the effective temperature at constant mass (Baraffe et al. 1997), with the magnitude of the effect decreasing toward the substellar boundary. However, it is not clear what happens in the lower-mass regime where degeneracy effects may alter the situation. Since no evolutionary models exist for sub-solar metallicity, substellar objects, we cannot provide a quantitative analysis of the evolutionary effect of slightly sub-solar metallicity. As discussed in Sect. 4, studies of the parent main-sequence star, ϵ Indi A, derive a metallicity in the range $[\text{Fe}/\text{H}] = -0.23\text{--}+0.06$, with the most recent study supporting $[\text{Fe}/\text{H}] = -0.2$. The effects of lower metallicity and increasing surface gravity are somewhat complementary, so we compare our observations with BT-Settl models of surface gravity from $\log g = 5.00$ to 5.50

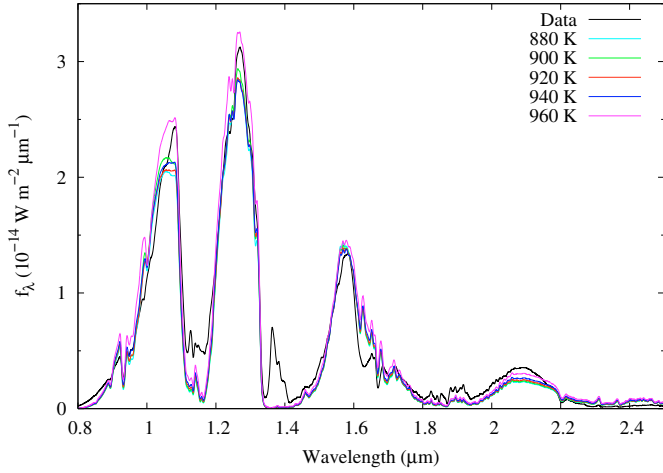


Fig. 18. Near-IR spectrum of ε Indi Bb (black line) with sub-solar metallicity ($[M/H] = -0.2$) BT-Settl spectra with $T_{\text{eff}} = 880, 900, 920, 940, 960$ K and $\log g = 5.25$ (cyan, green, red, blue, and magenta lines respectively). All spectra have been smoothed to 60 \AA FWHM and the observed spectrum median filtered to remove the lowest signal-to-noise points.

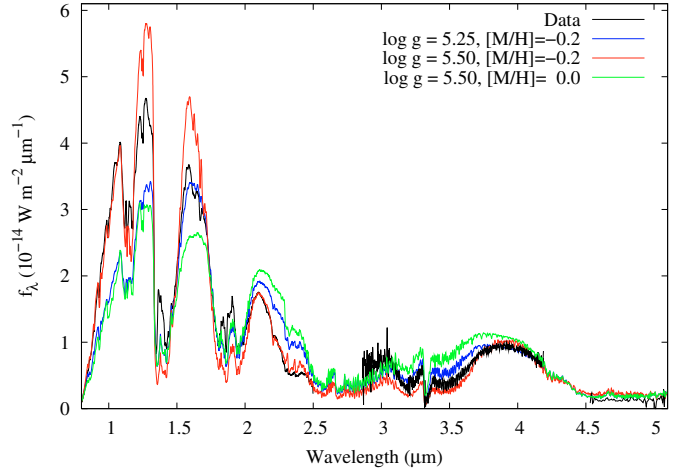


Fig. 20. Near- to thermal-IR spectra of ε Indi Ba (black line), the BT-Settl spectrum ($T_{\text{eff}} = 1320$ K, $\log g = 5.50$, $[M/H] = -0.2$, red line), the same with $\log g = 5.25$ (blue line), and with $\log g = 5.50$ but with solar metallicity ($[M/H] = 0.0$, green line). All spectra have been smoothed to 60 \AA FWHM and the observed spectrum median filtered to remove the lowest signal-to-noise points.

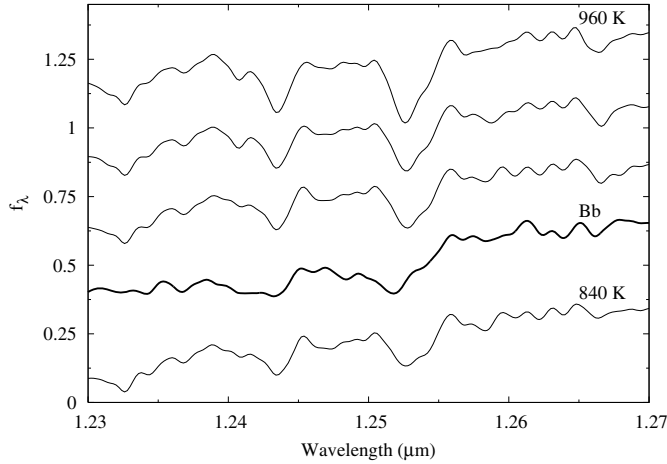


Fig. 19. $1.23\text{--}1.27 \mu\text{m}$ spectrum of ε Indi Bb (thicker line, second from bottom) and the $[M/H] = -0.2$, $\log g = 5.25$ BT-Settl spectra with $T_{\text{eff}} = 840\text{--}960$ K (increasing bottom to top in steps of 40 K). All spectra have been normalised and offset for clarity. All spectra have been smoothed to 10 \AA FWHM for easier comparison.

and with solar ($[M/H] = 0.0$) and slightly sub-solar metallicity ($[M/H] = -0.2$).

Figure 20 shows the near- to thermal-IR spectrum of ε Indi Ba compared to models with an effective temperature of 1320 K, surface gravities $\log g = 5.25$ and 5.50, and metallicities of $[M/H] = 0.0$ and -0.2 . The effect of higher metallicity and lower surface gravity is shown to be most prominent in the J - and H -bands. The flux in the 1.1 , 1.25 , and $1.6 \mu\text{m}$ peaks is suppressed, while the $2.2 \mu\text{m}$ peak flux is over-estimated. Additionally, the shape of the K - and L -bands is inconsistent with the observed spectrum. We find the higher surface gravity ($\log g = 5.50$) and sub-solar metallicity ($[M/H] = -0.2$) to be the better fit to the spectrum of ε Indi Ba.

Figure 21 shows the near-IR spectrum of ε Indi Bb compared to models with an effective temperature of 920 K, surface gravities $\log g = 5.00$ and 5.25 cm s^{-2} , and metallicities of $[M/H] = 0.0$ and -0.2 . We neglect the longer wavelength data here as the models show little variation. As with the comparison

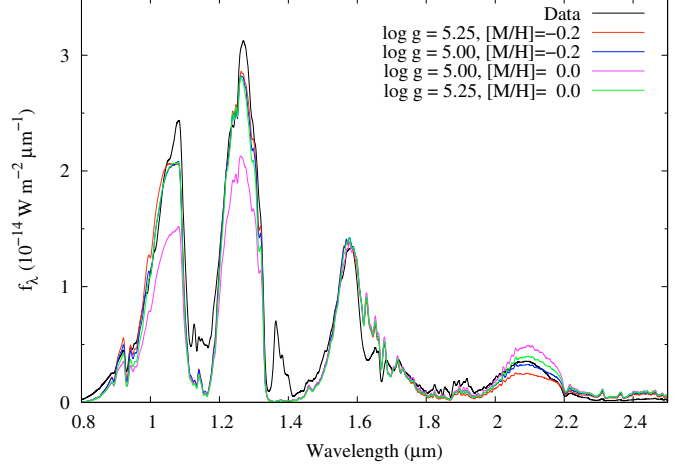


Fig. 21. Near-IR spectra of ε Indi Bb (black line), the BT-Settl spectrum ($T_{\text{eff}} = 920$ K, $\log g = 5.25$, $[M/H] = -0.2$, red line), the same with $\log g = 5.00$ (blue line), with $\log g = 5.00$, $[M/H] = 0.0$ (magenta line), and $\log g = 5.25$, $[M/H] = 0.0$ (green line). All spectra have been smoothed to 60 \AA FWHM and the observed spectrum median filtered to remove the lowest signal-to-noise points. The thermal-IR spectra have not been shown as there is little to distinguish between models.

of models with different effective temperatures, we find the H -band is relatively invariant to the different surface gravities and metallicity. The effects of surface gravity and metallicity are most apparent in the J - and K -bands. The general trend for dust-free T dwarfs such as ε Indi Bb is well established (cf. Leggett et al. 2009): both the lower metallicity and higher gravity result in higher atmospheric pressures, favouring the formation of methane and increasing collision induced absorption (CIA) opacity around $2 \mu\text{m}$.

The solar metallicity model with surface gravity $\log g = 5.00$ is the most inconsistent with our observations as the 1.1 and $1.25 \mu\text{m}$ peaks are significantly under-estimated while the $2.1 \mu\text{m}$ peak is significantly over-estimated. As explained earlier (see Sect. 8), we have chosen to use the Grevesse & Noels (1993) abundances which is likely the cause of the differences seen between our solar metallicity model spectra and those used

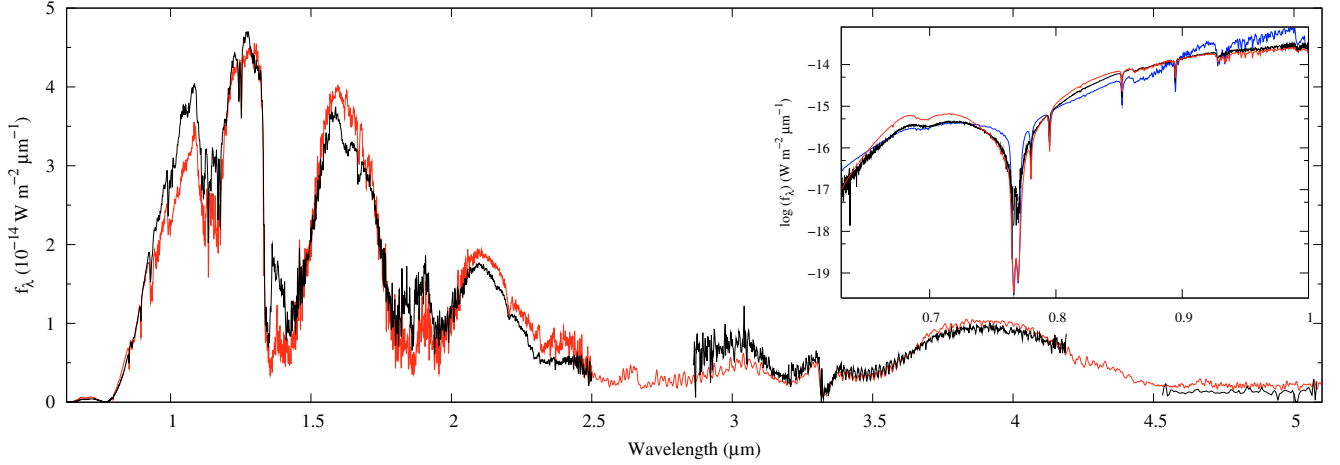


Fig. 22. Optical to thermal-IR spectrum of ε Indi Ba (black line) and the best-fit BT-Settl spectrum (red line, $T_{\text{eff}} = 1300$ K, $\log g = 5.50$, $[M/H] = -0.2$). Here the optical and near-IR data have been smoothed to 17 \AA FWHM and median filtered to remove the lowest signal-to-noise points. The model has been smoothed to 60 \AA FWHM beyond $2.5 \mu\text{m}$. Inset: the optical portion of the spectra smoothed to 6.5 \AA FWHM shown with the flux on a logarithmic scale. Also shown is a model fit to the optical spectrum with depleted alkali abundances (blue line). For this early T-dwarf, the standard alkali abundances provide the better match to the observed flux levels and spectral morphology. Additionally, the lithium abundance has been reduced by a factor of 1000 to allow a comparison with the observations which show no detectable lithium at 6707 \AA .

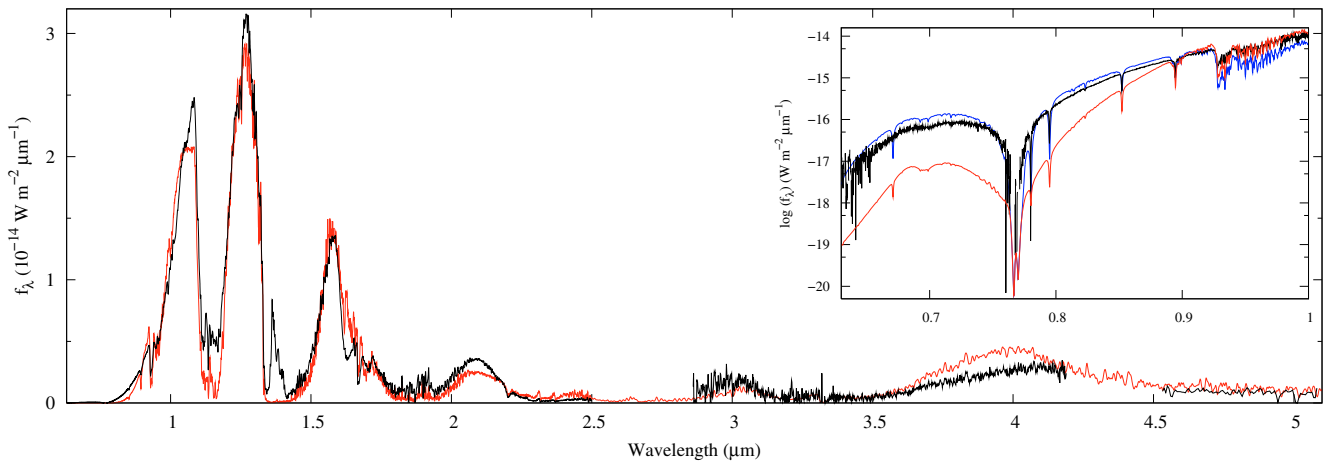


Fig. 23. Optical to thermal-IR spectrum of ε Indi Bb (black line) and the best-fit BT-Settl spectrum (red line, $T_{\text{eff}} = 920$ K, $\log g = 5.25$, $[M/H] = -0.2$). The spectra have been smoothed as in Fig. 22. For this late T-dwarf, the depleted alkali model provides the better match to the observed flux levels and spectral morphology in the optical which may be an indication of the formation of feldspars in late-T dwarfs which is not evident in earlier types. No lithium depletion has been implemented in these models.

in Kasper et al. (2009). The other models make very similar predictions to one another, except in the K -band. Although from Fig. 21, the $\log g = 5.00$, $[M/H] = -0.2$ model is marginally favoured, the comparison to all models within the effective temperature range of $880\text{--}940$ K favours $\log g = 5.25$, $[M/H] = -0.2$. Additionally, none of the models can reproduce the lower flux seen in the $2.2\text{--}2.5 \mu\text{m}$ region.

In summary, we find BT-Settl atmosphere models with effective temperatures in the range $1300\text{--}1340$ K, surface gravity of $\log g = 5.50$, and slightly sub-solar metallicity of $[M/H] = -0.2$ are the most reasonable fits to the observed optical to thermal-IR spectrum of ε Indi Ba. In Fig. 22 we show the 1300 K spectral model compared to the data. It is clear that this model does not provide a perfect match to the near-IR peaks, however general features are reproduced. The inset plot shows the mismatch in the shape of the KI profile at $0.77 \mu\text{m}$ which may suppress the continuum to beyond $1 \mu\text{m}$ (Burrows et al. 2000)

and so affect the relative strengths of the $1.1 \mu\text{m}$ and $1.25 \mu\text{m}$ peaks. Although the flux in the $2.8\text{--}3.2 \mu\text{m}$ region is underestimated, the $3.3\text{--}4.2 \mu\text{m}$ region is well-reproduced. However, in the M -band the model predicts higher fluxes than observed, suggesting insufficient understanding of the sources of opacity.

For ε Indi Bb, we find the BT-Settl models with effective temperatures of $880\text{--}940$ K, surface gravity of $\log g = 5.25$, and metallicity of $[M/H] = -0.2$ provide the best match to the observations. Figure 23 shows the 920 K model does not provide a perfect match to the near-IR peaks, although this is less pronounced than for Ba. The inset plot shows the large mismatch in the shape and flux level of the KI profile at $0.77 \mu\text{m}$ and the effect of employing a model with depleted alkali absorption. This effect is also evident in the optical colour-magnitude diagram of Fig. 14 where ε Indi Bb falls ~ 1.5 mag redward of the COND03 evolutionary models. We return to discuss the cause of this large effect in Sect. 8.4. The mismatch around $1.62\text{--}1.74 \mu\text{m}$

is mainly due to incomplete knowledge of CH_4 absorption in this range. In the 2.8–3.5 μm region, the shape of the spectrum due to CH_4 absorption is not well fit. In particular, the drop in flux predicted at $\sim 4.1 \mu\text{m}$ is not observed, and the M -band flux is again over-estimated.

The KI- H_2 quasi-molecular satellite feature at $\sim 0.69 \mu\text{m}$ discussed in Allard et al. (2007) is seen here in both ε Indi Ba and Bb (inset plots of Figs. 22 and 23). The shape of the feature is not perfectly reproduced, mainly because the effects of KI-He absorption have yet to be included. To a lesser extent, the ill-fitting wings of the very wide, pressure-broadened absorption lines of K I at 0.77 μm and Na I at 0.59 μm may also play a role.

8.3. Unidentified feature at 1.35–1.40 μm

We note a spectral feature at ~ 1.35 – $1.40 \mu\text{m}$ in the spectra of both ε Indi Ba and Bb which is poorly reproduced by the BT-Settl models (see Figs. 22 and 23) and has not been identified in all spectra of the T dwarf standard stars. Many observers remove this region from published spectra due to the high telluric absorption and so there are few available comparisons. Nevertheless, the region contains valuable information on the continuum flux level in these deep absorption bands present in T dwarfs. A similar feature is however seen in the spectrum of the T1 spectral standard SDSS0151+1244 (Burgasser et al. 2006b), the T8.5 and T9 dwarfs ULAS1238 and ULAS1335 (Burningham et al. 2008), and some L dwarfs (e.g. 2MASS J1507–1627 (L5), Burgasser 2007).

While this feature could be caused by problems with the telluric correction in this region, we believe that it may be intrinsic to these objects. We are satisfied that this feature is not an artefact of our spectral extraction. The rise in flux occurs part way through the last of the seven spectral orders which were combined to produce our J -band spectrum (see Appendix C), so the shape is not due to a scaling mismatch between adjoining regions. This region corresponds to the gaps in our standard star spectrum where high telluric absorption required replacement by the solar model of Kurucz (see Sect. 2.6), but this is not the cause of the feature, as the solar model has only weak spectral features here.

The BT-Settl model for ε Indi Ba shows some structure in the deep water bands between the J and H peaks that is qualitatively similar to the observed feature, though the flux is underestimated by a factor of ~ 2 . In the ε Indi Bb model the disagreement is much worse, with about an order of magnitude mismatch between the modelled feature (which is nearly invisible at the scale of Fig. 23) and the observation. Still, this suggests that the feature is due to the structure of the strongest part of the water absorption bands, which in this part of the spectrum form fairly high up in the atmosphere, corresponding to optical depths of $\tau_{\text{Rosseland}} = 0.1$ – 1.0 and temperatures of 700–1000 K. Incidentally, two other features which also have systematically underestimated flux in the present models form at a similar level, namely the collisionally-induced absorption (CIA) capping the flux peak in the K band, and the wings of the potassium doublet centred on 0.77 μm (see Sect. 8.4). A possible explanation for the mismatch in all these cases might be an underestimated local temperature, and thus source function, at this atmospheric level. A toy model indicates that an increase in temperature of 200–400 K could reconcile the modelled and observed flux levels, but at this point we have no reasonable idea for the cause of such heating (e.g. for an additional opacity source causing a corresponding back-warming). A full explanation of this feature

must also account for the apparent difference in strength between objects of the same spectral type.

8.4. Alkali depletion

The optical spectra of T dwarfs are dominated by alkali resonance lines which are the result of a balance between the increased transparency of the atmospheres, due to the progressive sedimentation of condensates, and the depletion of alkali metals from the gas phase, also due to condensation processes. It has been noted (Lodders & Fegley 2006; Burrows 2009) that alkali metal depletion cannot occur above $T \sim 1400$ K, below the condensation temperatures of most refractory species and furthermore, the first condensates are the feldspars ($[\text{Na,K}]\text{AlSi}_3\text{O}_8$) which require aluminium and silicon to form. However, in a stratified atmosphere, the latter elements can be expected to have already been depleted by higher-temperature condensates before feldspars would have a chance to form. In that case, the alkali elements could only condense into sulfides and halides (mostly Na_2S , KCl) at temperatures around 1000 K.

In any case, for mid- to late-type T dwarf atmospheres, the depletion of the sodium and potassium is not adequately accounted for in current models. At the higher temperatures of early T dwarfs such as ε Indi Ba, the standard BT-Settl model reproduces the shape and flux level of the K I doublet at 0.77 μm (and the red edge of the NaD line at 0.589 μm) reasonably well as shown in Fig. 22 (inset), but over-estimates the absorption in the later type ε Indi Bb by an order of magnitude (Fig. 23, inset, red line).

The line wings of the K I resonance doublet at 0.77 μm extend several 1000 Å and thus potentially suppress the flux out to the 1.1 and even 1.25 μm peaks. As pointed out already by Burrows et al. (2000), these line profiles show strong deviations from classical Lorentzian wings and thus require a more sophisticated broadening theory. Detailed spectral models of the alkali lines have been successfully used to model the optical spectrum of ε Indi Ba by Allard et al. (2007), based on improved interaction potentials with H_2 and He for the line profiles, and an earlier version of the settling framework to calculate the depth-dependent abundances of neutral alkali atoms. They were also able to identify the quasi-molecular satellite of K I seen in our resolved spectra (see Figs. 22 and 23). While the overall agreement of the modelled optical spectrum for ε Indi Ba is fair, the Bb model, though showing the same general features, underestimates the observed flux by up to an order of magnitude. Since the lines in both brown dwarfs should form at quite similar temperature levels, it is extremely unlikely that the line profiles are off by such a large amount for the cooler component only. One possible explanation for the mismatch is that the K I in the gas phase is much less abundant than expected from the settling model.

If we therefore consider additional condensation of the alkali metals into feldspars, which would result in alkali depletion from the gas phase at somewhat higher temperatures than in current models, we can bring the ε Indi Bb spectrum into reasonable agreement with observations as shown in Fig. 23 (inset, blue line). However in this case the fit to the ε Indi Ba spectrum becomes worse. The formation of feldspars implies that Al and Si would still have to be present in sufficient quantities at the feldspar condensation level and, indeed, recent calculations using results from updated RHD simulations (Freytag et al. 2010; Homeier et al., in prep.) imply that the upmixing of these species might be more efficient than previously assumed. Thus we

suggest that feldspar formation can efficiently deplete these species at the temperatures of mid-late T dwarfs.

8.5. Lithium

The presence and state of lithium in the atmospheres of brown dwarfs is governed by mass, present effective temperature, and age. The models of D’Antona & Mazzitelli (1994), Chabrier et al. (1996), and Burke et al. (2004) predict that a brown dwarf must have a mass greater than $0.060\text{--}0.065 M_{\odot}$ to be capable of reaching the core temperature of $\sim 3 \times 10^6$ K (Bildsten et al. 1997) required for lithium depletion (${}^7\text{Li} + p \rightarrow {}^4\text{He} + {}^4\text{He}$). Therefore, since objects less massive than $\sim 0.4 M_{\odot}$ are fully convective, all lithium should have been processed for any brown dwarf above $0.065 M_{\odot}$. Chabrier et al. (1996) predict that an object at this mass boundary will deplete its primordial lithium by a factor of 100 in ~ 1 Gyr, with faster depletion in higher-mass objects.

Furthermore, the substellar chemistry models of Lodders & Fegley (2006) show that LiI is the dominant form of lithium down to ~ 1520 K at 1 bar pressure (with the temperature limit increasing with increasing pressure), beyond which lithium is bound into molecules (LiCl, LiOH, etc.). Kirkpatrick et al. (2000, 2008) presented spectra of a number of L dwarfs with and without LiI absorption. They showed that the strength of the LiI 6708 Å line peaks at L6 and is observed in some L7 and L8 dwarfs with the strength of the line and number of detections decreasing toward later types.

Here we have higher resolution and higher signal-to-noise data and, from the observed spectral type-equivalent width relation of Kirkpatrick et al. (2000), we would have expected to detect LiI at 6708 Å in ϵ Indi Ba if it were present, but not necessarily in ϵ Indi Bb. Indeed, Burrows et al. (2002) state that there is no apparent reason why LiI would not be seen in objects as late as T6 with high enough quality data.

On the other hand, the presence of LiI absorption in our current atmospheric models may be due to unrealistic modelling of the removal of solid species from the atmosphere after formation (Marley, pers. comm.). As can be seen in the Fig. 24, we find no evidence for absorption by monatomic lithium at 6708 Å in the spectrum of ϵ Indi Ba, while the spectrum of ϵ Indi Bb may have inadequate signal-to-noise at this wavelength to judge its presence or absence at the low abundance levels expected for T6 dwarfs. To approximately quantify the level of lithium depletion, our models for ϵ Indi Ba must have the proto-solar lithium abundance reduced by a factor of at least 1000 (see Fig. 24) in order to reproduce the data.

The level of lithium depletion in ϵ Indi Ba is compatible with a mass in excess of $0.065 M_{\odot}$ ($68 M_{\text{Jup}}$). The less luminous ϵ Indi Bb on the other hand, must be less massive than this limit, and given its lower temperature, has most probably lost its atomic lithium to molecules.

8.6. Chemical equilibrium departures

At the effective temperatures of ϵ Indi Ba and Bb, carbon would be expected to be predominantly locked in carbon monoxide (CO) in the hotter, lower layers of the atmosphere, and in methane (CH₄) in the cooler, upper regions under chemical equilibrium (CE) conditions. However, since the detection of the CO fundamental band in Gl 229B by Noll et al. (1997), observational evidence has accumulated that CO persists in the upper atmospheres of T dwarfs in excess of its CE abundance.

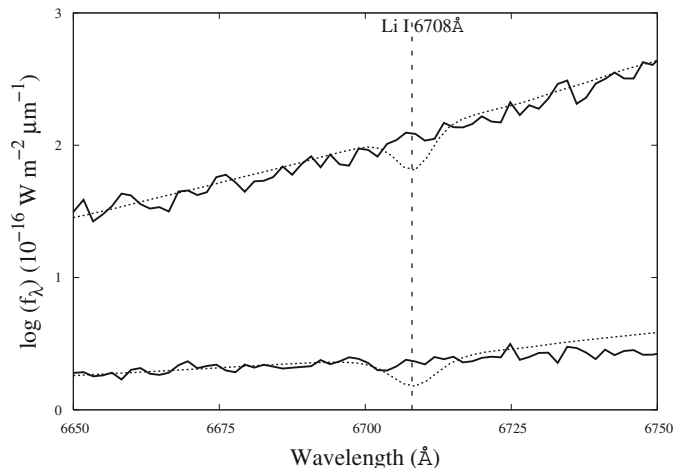


Fig. 24. The 6650–6750 Å spectra of ϵ Indi Ba and Bb (upper and lower thick black lines, respectively) and the BT-Settl models with $T_{\text{eff}} = 1300$ K, $\log g = 5.50$, and $[M/H] = -0.2$ (upper dotted line) and $T_{\text{eff}} = 920$ K, $\log g = 5.25$, and $[M/H] = -0.2$ (lower dotted line). Both models have been smoothed to 6.5 \AA FWHM to match the observations. The lithium abundance has been reduced by a factor 1000 in the $T_{\text{eff}} = 1300$ K model in order to provide a meaningful upper limit to the observed levels of LiI absorption in the spectrum of ϵ Indi Ba.

Griffith & Yelle (1999) and Saumon et al. (2003) have shown that this excess can be explained by the upmixing of CO from the warm deeper layers, since if one assumes sufficiently efficient turbulent mixing in the upper atmosphere, the kinetic rates for the conversion reactions from CO to CH₄ are too slow to adjust the mixing ratios to CE abundances. The BT-Settl models employ a similar calculation of these CE departure effects, but using diffusion coefficients derived from the CO5BOLD radiation hydrodynamics simulations (Freytag et al. 2010) rather than adjusting them as a free parameter (Homeier et al., in prep.). The diffusion coefficients thus calculated are therefore height-dependent and not directly comparable to a single choice of an eddy diffusion coefficient, with typical values in our models ranging between 10^5 and $10^9 \text{ cm}^2/\text{s}$. Since the CE departure is most sensitive to the mixing at the temperature level relevant for the transition from CO to CH₄, i.e. between 1000 and 1500 K, the diffusion coefficient in this part of the overshoot region would best characterise our model, corresponding to $10^7\text{--}10^8 \text{ cm}^2/\text{s}$ in the ϵ Indi Ba model. In addition, we consider several reaction pathways and timescales besides the one from Prinn & Barshay (1977), on which the Saumon et al. (2003) models are based, notably the revised time scale for the scheme of Prinn & Barshay (1977) suggested by Griffith & Yelle (1999), and the reaction scheme of Yung et al. (1988) (see also Griffith & Yelle 1999). Among these, the Yung et al. (1988) model generally predicts the fastest conversion rates from CO to CH₄, and the Prinn & Barshay (1977) model with the modified rates of Griffith & Yelle (1999) the slowest rates, implying the strongest CE departure effects.

Since the velocity field derived from the CO5BOLD simulations is used for the description of both the cloud dynamics and the CE departures, these models employ a high degree of self-consistency, with any change in the mixing properties immediately affecting both the dust content and the gas-phase chemistry of the atmosphere. On the other hand, other potential uncertainties in our cloud model would also feed back into the thermal profile of the atmosphere and might thus affect the domains of different carbon chemistry discussed above. However, any major

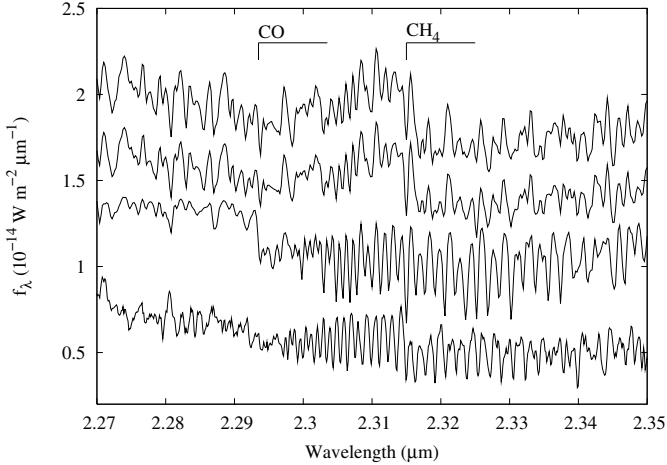


Fig. 25. The 2.27–2.35 μm spectrum of ε Indi Ba (bottom line) showing the CO 2–0 overtone along with models employing different chemical equilibrium (CE) timescales. All models have $T_{\text{eff}} = 1320$ K, $\log g = 5.50$, and $[\text{M}/\text{H}] = -0.2$. A chemical equilibrium model is shown at the top, the Prinn & Barshay (1977) model second from bottom, and a model following the Yung et al. (1988) chemistry second from top. All models have been smoothed to 4.9 \AA FWHM to match the observations. The ε Indi Ba spectrum shows the absolute flux scale, while the Prinn & Barshay (1977), Yung et al. (1988) and CE models have been offset for clarity by 0.1, 0.8, and 1.0, respectively.

changes in cloud opacity would also inevitably change the spectral energy distribution and thus produce inconsistencies with the observed IR photometry. As the overall fit to the spectral energy distribution is good, we thus feel confident that our chemistry model is not affected by major uncertainties in the thermal structure due to backwarming from the cloud deck.

As an L–T transition object, marking also the transition from CO-dominated to CH_4 -dominated chemistry, ε Indi Ba is particularly sensitive to the reaction details discussed above. The high quality of the present *K*- and *L*-band spectra thus allow quantitative estimates of the CO and CH_4 mixing ratios, enabling us to directly test these models of the non-equilibrium chemistry and constrain the relevant timescales. Figure 25 shows the observed 2.27–2.35 μm spectrum, where the CO 2–0 overtone band (starting at 2.2935 μm) can be identified even on top of the octad band of CH_4 . For comparison, a chemical equilibrium model and non-CE model spectra, based on the reaction models of Prinn & Barshay (1977) and Yung et al. (1988) respectively, are shown. The Prinn & Barshay (1977) model better reproduces the rotational series of the CO 2–0 R branch extending redwards from 2.2935 μm , but the CE and Yung et al. (1988) models match the overall morphology better, including the 2.315 μm CH_4 bandhead. However, as seen in Fig. 26, the Prinn & Barshay (1977) model does not match the shape of the *L*-band spectrum, whereas the chemical equilibrium model and the Yung et al. (1988) model provide reasonable matches to the shape and absolute flux levels – the CH_4 absorption predicted by both models is identical within the internal uncertainties of the model atmospheres. Also shown is a model employing the Prinn & Barshay (1977) model with the revised reaction rates of Griffith & Yelle (1999) which shows an even poorer match to the spectral morphology, since in this model even less CH_4 has formed. However, the depth of the CH_4 absorption at ~ 3.3 μm falls between that seen in the spectra predicted by the Yung et al. (1988) and Prinn & Barshay (1977) models, just as the 2.3 μm spectrum indicates a CO abundance intermediate between those models. This would suggest that the

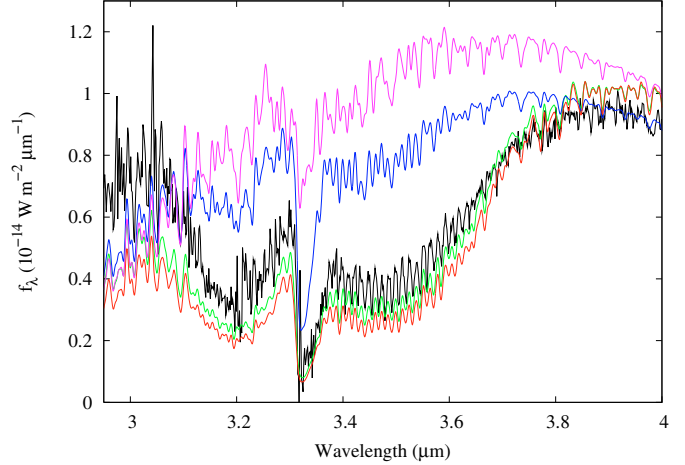


Fig. 26. The *L*-band spectrum of ε Indi Ba (black line) and different chemistry models with $T_{\text{eff}} = 1320$ K, $\log g = 5.50$, $[\text{M}/\text{H}] = -0.2$. A chemical equilibrium model is shown in green, the Prinn & Barshay (1977) model in blue, the Prinn & Barshay (1977) model with the revised reaction rates of Griffith & Yelle (1999) in magenta, and a model following the Yung et al. (1988) chemistry in red. All models have been smoothed to 60 \AA FWHM to match observations.

correct reaction timescale might have a value slightly below that of Yung et al. (1988), or alternatively, the vertical mixing could be more efficient than assumed in the BT-Settl models. Freytag et al. (2010) suggest such additional mixing can be produced by convectively driven gravity waves, though the mixing efficiency of such waves in terms of an equivalent diffusion coefficient is still under investigation.

Our observations provide only limited coverage and resolution of the strongest CO absorption feature, the 1–0 fundamental band at 4.55 μm (see Fig. 7). However, the resolution of our *M*-band spectra does not allow us to favour any model over the other. Although the models differ in the predicted absolute flux levels, none of these match the observed flux levels.

We have shown that the observed *K*-band spectrum of ε Indi Ba shows evidence of non-CE processes and the *L*-band spectrum supports a CO– CH_4 reaction rate intermediate between that predicted by the Yung et al. (1988) and Prinn & Barshay (1977) models. However, we postpone a more detailed analysis of the non-chemical equilibrium signatures to a future paper.

9. Mass limits on further system members

Using the previously derived flux limits from the deep imaging of the system (see Sect. 2.4) and an approximate system age of 5 Gyr, we can derive mass limits of further members using models. The COND03 models rule out any system members of mass greater than $15 M_{\text{Jup}}$ ($H = 19.1^{\text{m}}$) in the field around ε Indi Ba, Bb (7–39.7 AU), and also rule out objects more massive than $34 M_{\text{Jup}}$ ($H = 15.8^{\text{m}}$) from 7 AU down to 0.8 AU from either Ba or Bb. If the system were as young as 1 Gyr, the corresponding mass limits would be 6.0 and $13 M_{\text{Jup}}$, respectively.

At separations less than 1–2 FWHM (~ 0.4 – 0.8 AU), our ability to distinguish companions of Ba or Bb is limited by the high object flux and pixelation of the PSF. However, if either ε Indi Ba or Bb had substantial unresolved companions, then their combined observed spectra would be notably different compared to the spectral standards. The combined spectrum of ε Indi Ba and Bb is drastically different to that of Ba alone,

so any additional companion must be significantly fainter, and hence less massive, than Bb.

10. Comparison of model predictions

10.1. Previous determinations

Observations of ε Indi Ba, Bb have previously been compared to different atmospheric and evolutionary models. [Smith et al. \(2003\)](#) used $R \sim 50\,000$ spectra in the ranges $1.553\text{--}1.559\ \mu\text{m}$ and $2.308\text{--}2.317\ \mu\text{m}$ to derive an effective temperature for ε Indi Ba from comparisons of the observed spectra with spectral models to fit bands of CO and H₂O. They derived effective temperatures of 1400 K and 1600 K from the two regions and so adopted 1500 K as the effective temperature of ε Indi Ba. As they note, this is significantly in excess of that derived in other analyses, and the temperatures derived from the two regions are inconsistent. Moreover, the effective temperature of 1600 K derived for the $2.308\text{--}2.317\ \mu\text{m}$ region may be affected by the CO/CH₄ chemistry.

[Roellig et al. \(2004\)](#) and [Mainzer et al. \(2007\)](#) observed the combined spectrum of the ε Indi Ba, Bb system using IRS on *Spitzer*. Using the luminosities of [McCaughrean et al. \(2004\)](#) and an age of ~ 1 Gyr, they derived evolutionary model parameters of $T_{\text{eff}} = 1210$ K, $\log g = 5.10$ (for a cloudy evolutionary model) and $T_{\text{eff}} = 840$ K, $\log g = 4.89$ for ε Indi Ba and Bb, respectively. Using these parameters along with radii of 0.094 and 0.100 R_{\odot} for ε Indi Ba and Bb, respectively, [Roellig et al. \(2004\)](#) and [Mainzer et al. \(2007\)](#) generated a composite model spectrum which agreed well with the observed combined spectrum. However, [Sterzik et al. \(2005\)](#) presented mid-IR photometry of the individual sources from VLT/VISIR which they suggest is not compatible with the absolute fluxes of the individual models from [Roellig et al. \(2004\)](#). Indeed, as pointed out in Sect. 5, the *Spitzer* and VISIR fluxes differ significantly. Using an assumed age of 1 Gyr, [Sterzik et al. \(2005\)](#) found an effective temperature of 1100 K for ε Indi Ba. However, our comparison of the optical to thermal-IR spectrum excludes such low effective temperatures.

Finally, [Kasper et al. \(2009\)](#) used low resolution near-IR spectroscopy and the models of [Burrows et al. \(2006\)](#) to yield effective temperatures of 1250–1300 K and 875–925 K and surface gravities of 5.2–5.3 and 4.9–5.1, for ε Indi Ba and Bb, respectively. These temperatures are broadly comparable to ours, although in more detail we find the BT-Settl spectral models cannot match the observed ε Indi Ba spectra at effective temperatures as low as 1250 K. Their grid of surface gravity was finer than used here and they derive values significantly lower than ours. For ε Indi Ba, we have compared our observations to models with $\log g = 5.25$ and 5.50, and specifically prefer the higher value. Similarly, for ε Indi Bb, we have tested models with $\log g = 5.00$ and 5.25, and again prefer the higher value. The various determinations of the effective temperatures of ε Indi Ba and Bb are summarised in Table 9.

The situation is complicated by complementary effects on the spectral morphology due to surface gravity, metallicity, and elemental abundances. We do not believe that the surface gravity can be constrained to better than ~ 0.25 dex. More precise determinations of the surface gravity can lead to substantially inaccurate predictions of the mass as in [Kasper et al. \(2009\)](#), which may do the evolutionary models an injustice. Indeed, [Burrows et al. \(2006\)](#) suggest that the lack of a detailed understanding of brown dwarf meteorology may lead to ambiguity in derived effective temperatures of $\sim 50\text{--}100$ K and surface gravities and ~ 0.3 .

Table 9. Comparison of our model predictions with previous studies.

Study	ε Indi Ba T_{eff}	ε Indi Bb T_{eff}
Smith et al. (2003)	1400,1600	...
Roellig et al. (2004)	1250	800
Sterzik et al. (2005)	1100	...
Mainzer et al. (2007)	1250	800
Kasper et al. (2009)	1250–1300	875–925
This work (atm. models)	1300–1340	880–940
This work (evo. models)	1352–1385	976–1011

The last two entries show the determinations of the effective temperatures of the two T dwarfs from this work, both from fitting atmospheric models to the observed spectra, and by comparing the derived luminosities and dynamical system mass with evolutionary models.

[Kasper et al. \(2009\)](#) used their fitted effective temperatures and surface gravities to derive ages and masses from the evolutionary models of [Burrows et al. \(1997\)](#). For ε Indi Ba, they found an age of 1.0–2.3 Gyr and mass of 46–62 M_{Jup} , and for ε Indi Bb an age of 1.0–2.0 Gyr and a mass of 29–39 M_{Jup} . Although the objects appear to be co-eval and consistent with the age estimate of [Lachaume et al. \(1999\)](#), this age range is clearly lower than we have derived in the present paper using the observed luminosities and dynamically derived system mass. Additionally, their predicted total maximum system mass (101 M_{Jup}) is considerably lower than the measured system mass (121 M_{Jup}). This suggests that either there are large systematic errors in the evolutionary model predictions, or the effective temperatures and surface gravities derived from observed spectra are inaccurate. This comparison highlights the problems associated with deriving the physical properties of other field objects for which we do not have a comprehensive set of observations or external constraints from a companion star.

10.2. Our model predictions

Our comparison of the observed luminosities and measured total mass of ε Indi Ba, Bb has allowed us to derive a predicted age range of 3.7–4.3 Gyr from the COND03 evolutionary models. While this age range is higher than the previously used age estimate of 0.8–2.0 Gyr from [Lachaume et al. \(1999\)](#), it is younger than other age indicators for ε Indi A in the literature discussed in Sect. 7.3. From this age range and the individual luminosities we have extracted the predicted individual masses, effective temperatures, radii, and surface gravities (see Table 7). The effective temperatures predicted by these models are 1352–1385 K for ε Indi Ba, and 976–1011 K for Bb with surface gravities of 5.43–5.45 and 5.27–5.33.

We have also independently derived the effective temperature and surface gravity of both objects through a direct comparison of the observed optical to thermal-IR spectra with the BT-Settl atmospheric models. For ε Indi Ba, we found models with effective temperature in the range 1300–1340 K and surface gravity of $\log g = 5.50$ are the most appropriate, while for ε Indi Bb we find effective temperatures in the range 880–940 K with surface gravity of $\log g = 5.25$, both with slightly sub-solar metallicity of $[M/H] = -0.2$.

We cannot presently reconcile the effective temperatures derived from atmospheric modelling with those derived from evolutionary models using the measured system mass at the observed luminosities. However, it must be noted that the evolutionary models do not presently incorporate the new BT-Settl atmospheres. The difference between the predicted

effective temperatures for ε Indi Bb show the atmospheric models to be inconsistent with the evolutionary models. The upper limit on the effective temperature from the comparison with atmospheric models is 940 K, while the evolutionary models predict effective temperatures of at least 975 K. For ε Indi Ba, the difference is less severe. There is only a 10 K difference between the limits on the effective temperature from the evolutionary and atmospheric models. This is midway between the effective temperature steps in our grid, although it is clear that by 1360 K the atmospheric models are no longer consistent with the spectroscopic observations. These differences may be resolved by the inclusion of the BT-Settl atmospheric models in the next generation of evolutionary models, as the effect on the effective temperature would presumably be intermediate between that of the COND03 and DUSTY00 models. However, we note that Dupuy et al. (2009) also find that the effective temperatures predicted using atmospheric and evolutionary models are in disagreement for the components of the L4+L4 binary HD 130948BC.

The derived surface gravities are consistent between the evolutionary and atmospheric models. However, due to the grid step chosen (0.25 dex) and the complementarity with metallicity, the surface gravities derived from the comparison of our observed spectra with the atmospheric models do not provide a strong test of the atmospheric and evolutionary model predictions. Additionally, any mass estimated from the radius determined for each spectral model, the fitted surface gravity and our derived luminosities, will give a large range of possible masses.

As described earlier, once the individual masses have been determined from the ongoing absolute astrometric monitoring Cardoso et al. (in prep.), we will be able to test the evolutionary models using the individual masses, luminosities, and the same age for both T dwarfs. Additionally, once more reliable age determinations become available we will be able to directly test the evolutionary models and determine if the luminosities are overestimated for intermediate age brown dwarfs as suggested by Dupuy et al. (2009) for the young system HD 130948BC.

For the observed luminosity of ε Indi Ba and effective temperature range of 1300–1340 K derived from the comparison to atmospheric models, the COND03 evolutionary model predicts a mass for ε Indi Ba in the range 46–64 M_{Jup} , and for ε Indi Bb in the range 16–37 M_{Jup} from its observed luminosity and the effective temperature range of 880–940 K. Given the preliminary dynamical system mass of $121 \pm 1 M_{\text{Jup}}$ (Cardoso et al. 2009a), it therefore appears that with current theoretical models and spectroscopically derived effective temperatures, one cannot obtain reliable mass predictions for T dwarfs such as these even when precise luminosity constraints are available.

11. Conclusions

We have presented the results of a comprehensive photometric and spectroscopic study of the individual components of the nearest known binary brown dwarf system, ε Indi Ba, Bb. The relative proximity of these T1 and T6 dwarfs to the Earth resulted in very high quality data, while archival results for the well-studied parent star, ε Indi A, provide invaluable additional information. We find the spectra of these brown dwarfs are best matched by the BT-Settl spectral models with $T_{\text{eff}} = 1300\text{--}1340$ K and $\log g = 5.50$ for ε Indi Ba and 880–940 K and 5.25 for ε Indi Bb, both with a metallicity of $[M/H] = -0.2$.

COND03 evolutionary model predictions for the masses are significantly inconsistent with the measured system mass if the young age range of 0.8–2.0 Gyr suggested by Lachaume et al. (1999) is used. We find that a system age of 3.7–4.3 Gyr is

necessary for the COND03 evolutionary models to be consistent with the measured system mass at the observed luminosities, and a review of the literature finds evidence supporting an age of ~ 5 Gyr for ε Indi A. In the age range 3.7–4.3 Gyr, the COND03 models predict effective temperatures in the range 1352–1385 K and 976–1011 K, for Ba and Bb, respectively.

It is clear that there are several areas in which the atmospheric models currently do not reproduce observations and a more detailed analysis of these issues will be the subject of future work. They include the strength and shape of the wide absorption by KI and NaI in the optical, the possible formation of feldspars in mid-late T dwarfs, and the reaction rates of CO and CH₄. In addition, the spectral shape in the L-band caused by CH₄ absorption is poorly reproduced, as is also the case for CH₄ absorption at $\sim 1.6 \mu\text{m}$. The M-band spectra, although low resolution, also show that the atmospheric models significantly over-estimate the flux in this region. While the flux levels of the near-IR peaks can be reasonably reproduced, the level of absorption between the peaks tends to be problematic. In particular, we find a feature at 1.35–1.40 μm in both our object spectra which is not predicted in the atmospheric models.

Neither source has detectable atomic LiI absorption at 6708 Å. The absence of lithium in the more massive component is consistent with the revised, higher age estimates coupled with its probable dynamical mass, while the lack of absorption in the cooler source is expected from its low effective temperature, where lithium is incorporated into molecules.

Although there is significant room for improvement in the atmospheric models, the current match to ε Indi Ba and Bb is nevertheless impressive. When new data on methane opacities become available, we will be able to better reproduce the observed spectra and more reliably compare these spectral models to spectra of objects with less well-constrained physical parameters. Additionally, when these updated atmospheric models are incorporated into the evolutionary models, a fully self-consistent comparison will be possible.

Finally, when the individual dynamical masses become available and if we can obtain a reliable estimate of the age of this system, based on asteroseismological observations of the parent star ε Indi A, then ε Indi Ba and Bb will become invaluable benchmark objects with a full set of physical parameters which newer models will have to reproduce, making them more reliable for analysing the properties of isolated ultra-cool field dwarfs.

The predictions of the evolutionary models using luminosity and mass constraints are somewhat different to the derived effective temperature and surface gravity from fitting atmospheric models to observed spectra. These differences may be resolved when the newer atmosphere models are incorporated into the evolutionary models. However, it seems that derivations of the mass of cool brown dwarfs are uncertain even where estimates of the effective temperature, surface gravity, and luminosity exist. We therefore caution against the over-analysis of predicted brown dwarf masses at this time.

Acknowledgements. NSO/Kitt Peak FTS data used here were produced by NSF/NOAO. R.R.K. acknowledges the support of an STFC studentship. Part of this work was funded by the European Commission Marie Curie Research Training Network CONSTELLATION (MRTN-CT-2006-035890). R.R.K. would like to thank Adam Burgasser, Mark Marley, Davy Kirkpatrick, and Sandy Leggett for useful discussion. This research has benefited from the SpeX Prism Spectral Libraries, maintained by Adam Burgasser at <http://www.browndwarfs.org/spexprism>. We thank Isabelle Baraffe for supplying the grid of evolutionary models and also the referee for helpful suggestions which improved the paper.

Appendix A: Image fitting with analytic functions

The 2-dimensional profile, or the point spread function (PSF), of ground-based optical/IR images is a superposition of several effects (Racine 1996), most importantly the spreading effect of the Earth's atmosphere caused by the mixing of air of different temperatures, leading to different refractive indices. In addition, there is the contribution of the optics and detectors used and any unintentional telescope motions, for example, due to imperfect tracking, which can cause elliptical profiles.

Various authors have attempted to produce an analytical function which represents the shape of the PSF (e.g. King 1971; Bendinelli et al. 1987). In a study of the two-dimensional profile of stellar images on photographic plates, Moffat (1969) found that a Gaussian profile, usually assumed to be a good match to the seeing, under-estimated the flux from the star at large radial distances. He proposed an analytical profile (now termed the Moffat profile) to be a better match to photographic stellar images. Similarly, King (1971) found that a Gaussian profile was not sufficient to match observations, proposing instead a profile composed of a Gaussian core, falling to an exponential which tails to a inverse-square aureole. Franz (1973) presented a further analytical representation of the PSF which is often referred to as a modified Lorentzian. This was later successfully applied to CCD images of stellar profiles by Diego (1985).

We used the Levenberg-Marquardt technique to extract the best-fit parameters for each of three different analytical PSF models: Gaussian, elliptical Moffat, and elliptical modified Lorentzian profiles, with the aim of extracting the ratio of the fluxes of the two objects, thus allowing individual magnitudes to be found. The pixelation of the profile was accounted for in the fitting routine by pixelating the model values to the same resolution as the data. The Moffat profile used is an elliptical version of the profile proposed by Moffat (1969):

$$M(r) = \frac{A}{[1 + B_{12}]^\beta}$$

$$B_{ij} = \left(\frac{r}{\alpha_{ij}} \right)^2 = \left(\frac{\cos^2 \theta}{\alpha_i^2} + \frac{\sin^2 \theta}{\alpha_j^2} \right) (x - x_0)^2 + \left(\frac{\sin^2 \theta}{\alpha_i^2} + \frac{\cos^2 \theta}{\alpha_j^2} \right) (y - y_0)^2 + \left(\frac{1}{\alpha_i^2} - \frac{1}{\alpha_j^2} \right) 2 \cos \theta \sin \theta (x - x_0)(y - y_0)$$

where A is the peak amplitude, (x_0, y_0) the central co-ordinates, and α_1, α_2 , and θ define the semi-major and semi-minor axes, and the position angle of the ellipse. The elliptical modified Lorentzian used followed that of Diego (1985):

$$L(x, y) = \frac{A}{[1 + B_{12}^{0.5\gamma(1+B_{34})}]},$$

where α_1 and α_2 are scale factors which relate to the full-width at half-maximum (Diego's RX and RY), and α_3 and α_4 are similar scale factors which allow the exponent of B_{ij} to vary with position (Diego's PRX and PRY).

In Table 1 we showed the flux ratio and uncertainty derived in each band for both objects along with the central wavelengths and widths of the observed filters. The uncertainty on the fitted amplitudes for each image was found from the covariance matrix calculated by the Levenberg-Marquardt fit, which is a reasonable estimate of the standard error when, as in this case, the χ^2 function is quadratic. However, the uncertainties on the reported flux

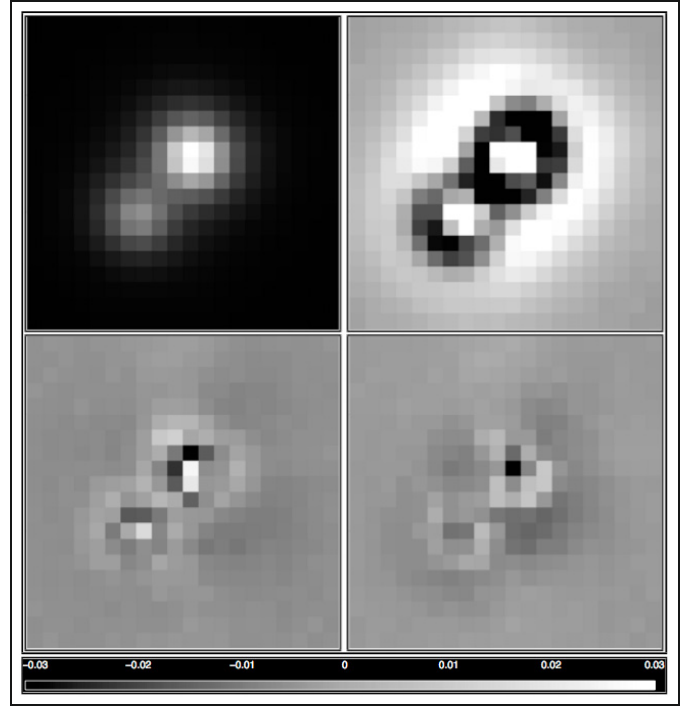


Fig. A.1. An ISAAC J -band image of the ϵ Indi Ba, Bb system (*top left*) and the residuals of the Gaussian (*top right*), modified Lorentzian (*bottom left*), and Moffat profile fits (*bottom right*). Each image is a 20×20 pixel ($2.96'' \times 2.96''$) sub-section of the full image. North is up, East left. The scale applies to the residual images and shows the flux as a fraction of the observed peak pixel flux. It is apparent that the Gaussian profile is the worst fit, while the Moffat profile is somewhat better than the Lorentzian.

ratios are the standard errors of the fits for all images for each filter, which were comparable to the uncertainties from the covariance matrix. The uncertainties on the flux ratios are not the dominant uncertainties in the final photometry of the two objects and so the anti-correlation is negligible.

The residuals of the best-fit profiles for each of the three functions are shown in Fig. A.1 for an example observation and demonstrate the suitability of each profile to match the data. The Gaussian is seen, as expected, to provide the worst fit, under-estimating the peak and wings while over-estimating in between as it attempts to match the entire profile. If this profile were used to fit the relative fluxes of isolated stars in an image, one would expect it to return reasonable results, but the inability of the Gaussian to determine the flux in the wings of an object which blends with the profile of another makes it ineffective at extracting relative photometry of blended objects. The residuals of the modified Lorentzian profile however, show much reduced levels, with the Moffat profile residuals even lower.

As confirmation of the validity of our PSF-fitting routine, it was employed to fit our optical images which we had previously fit with the DAOPHOT/IRAF algorithm of Stetson (1987). DAOPHOT uses an analytical profile to model the core of the PSF and builds up an empirical determination of the wings from the chosen model stars. Although not completely independent of our method, in that it too uses an analytical profile, it is the matching of the model PSF to the wings that allows DAOPHOT to accurately extract the flux of blended objects. We fit 5 images in the I - and z -band and 12 images in the R -band. Our fitting routine finds flux ratios of 4.71 ± 0.08 , 4.99 ± 0.05 , and 3.78 ± 0.08 for the R -, I -, and z -bands respectively, while with DAOPHOT

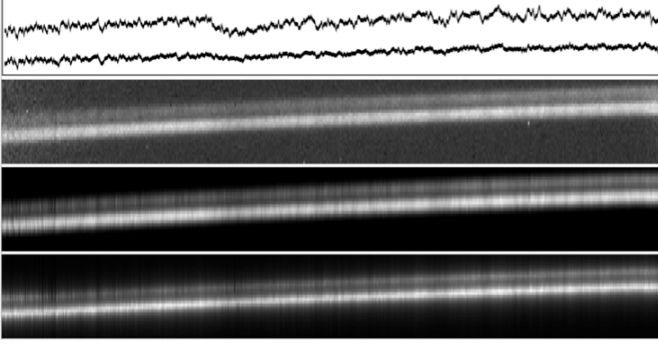


Fig. B.1. The top panel shows the spectrum of ε Indi Ba (upper line) and Bb in the region $0.975\text{--}1.022\ \mu\text{m}$ where absorption by FeH and CrH is present. The second panel from the top shows an image of the observed spectrum (ε Indi Ba is the lower spectrum) sloping across the detector. The third panel from the top shows the corresponding fitted double Gaussian profile and the bottom panel shows the fitted double Moffat profile. The vertical striping seen in the fits is an effect of utilising the signal of all the pixels in the spatial direction to increase the signal-to-noise and so detect fine spectral features.

we find flux ratios of 4.81 ± 0.07 , 5.04 ± 0.05 , and 3.85 ± 0.03 . The results of both PSF-fitting routines agree within the uncertainties in all cases, confirming the validity of our wholly analytical routine. Although the fitted flux ratio from DAOPHOT is larger than that from our fitting routine in these three examples, this is not true for all fitted images.

Appendix B: Spectral fitting routine

As with the imaging, the spectra of the two brown dwarfs were partially blended in the spatial direction and so a bespoke fitting algorithm was implemented to extract the individual spectra. The process was similar to the image fitting routine. We iteratively fit the parameters of a double Gaussian profile to the spatial direction at each column along the spectra. Initially all parameters are free, but after the first fit we calculate the mean of the separations of the two peaks at each wavelength step, weighted by the total flux at each wavelength, from the ~ 1000 profiles in each image and refit the profiles with the separation fixed. We then do the same to derive a global fit to the spatial $FWHM$ which we take to be constant with wavelength over each spectral window. The absolute position of the peaks at each wavelength was then constrained by a trace of the spectrum across the detector so that an accurate centre would be found even for wavelengths with little signal-to-noise. With these constraints, the remaining parameters were refit and the amplitudes were used along with the wavelength calibration to construct the individual wavelength-calibrated spectra.

We found that a double Gaussian profile provided the best fit to our spectroscopic data, unlike in our broadband imaging where a Moffat profile was preferred. Figure B.1 shows an image of the spectrum of ε Indi Ba, Bb in the region $0.975\text{--}1.022\ \mu\text{m}$, along with fitted spectra, one using Gaussian profiles, the other Moffat profiles. The apparent vertical striping in the fitted spectra are real spectral features revealed by using the entire profile to increase the signal-to-noise.

The resulting residuals for each profile (Fig. B.2) show clearly that the Gaussian profile is the better match. The Moffat profile under-estimates the peak of the profile while over-estimating the wings, consequently the contribution of the flux from one object to the other is not well determined. While an

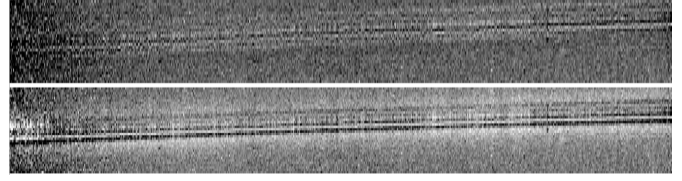


Fig. B.2. Residuals of the Gaussian (top) and Moffat profile fits to the spectral region shown in Fig. B.1. The ill-fitting wings of the Moffat profile suggest that it is not a good approximation for the spatial profile in our spectroscopic images, while the Gaussian profile residuals are almost consistent with the background noise.

analytical Gaussian profile should not in principle be an exact match to the observed stellar spectral profile, the residuals are almost consistent with the background noise. It may have been expected that the same profile would be preferred for the spectroscopy and broadband imaging, but if we consider imaging to be the integral of many Gaussian profiles with the $FWHM$ varying as a function of wavelength, then the result would not be truly Gaussian. Nevertheless, the residual images and spectra clearly favour different profiles. The resulting full resolution spectra are presented in Figs. 5–7.

Appendix C: Photometric calibration

To allow a meaningful comparison of our sources with other observed brown dwarfs, it is necessary to place the magnitudes on a common photometric system due to the differences between filter systems. In the near- to thermal-IR, the Mauna Kea Consortium filter-set (Tokunaga et al. 2002) has been chosen for this purpose by several groups (Stephens & Leggett 2004; Golimowski et al. 2004; Hewett et al. 2006) since these filters do not extend into the water absorption bands of the atmosphere and so avoid the large differences in relative spectral response between sites and from varying atmospheric conditions. The differences between the MKO JHK filters and the ISAAC JHK_S filters used for our observations are shown in Fig. C.1. Many observations have also been reported in the 2MASS system (Carpenter 2001) due to the large number of ultra-cool dwarfs found in the 2MASS database, although this system still encroaches on the regions of telluric absorption. We therefore present our near-IR photometry of ε Indi Ba, Bb in both MKO (Table 2) and 2MASS systems (Table 4) to allow easy comparison with other data. In the optical, we observed ε Indi Ba, Bb in the FORS2 Bessell V and I , the FORS2 R special, and the FORS2 Gunn z filters and report our photometry in the FORS2 system.

As none of our standard stars were of similar colour to our targets, when transforming our photometry into standard systems, we could not use standard colour equations, nor could we ignore colour terms due to the filter differences. This is clear from Fig. C.1 where we see that a T dwarf has relatively little flux in the regions of high absorption in the Earth’s atmosphere (due to the dominance of H_2O in both cases), but the standard star (in this case a solar-type star) will lose a large fraction of its flux in these regions. As a result, slight differences in the near-IR profiles of different systems can result in magnitude differences as large as 0.1^m (cf. Stephens & Leggett 2004).

In the near-IR, photometric calibration used the solar type star, S234-E (Persson et al. 1998), as our standard star in the JHK_S bands with the magnitudes known in the LCO (Las Campanas Observatory) system. HD 205772 (A3) and HR8042 (G3IV) were used in the L -band and M_{NB} -bands, respectively. The L -band standard star magnitude was known in

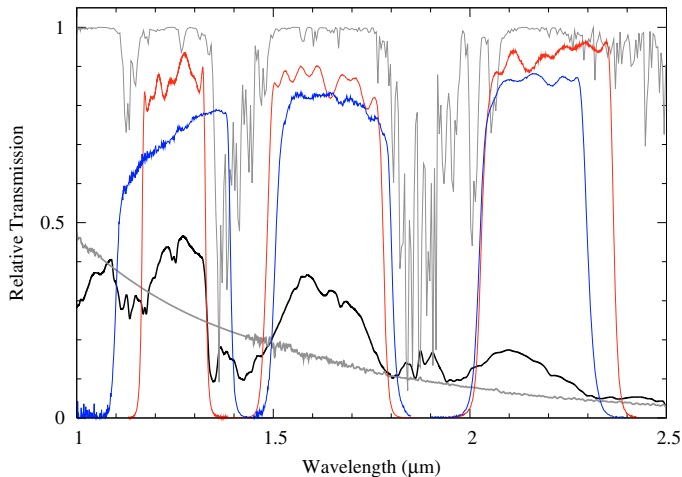


Fig. C.1. The *JHK* band-passes of the MKO filter-set (red lines) and the ISAAC *JHK_S* filter-set (blue lines). The top-most line (thin, grey line) traces a typical atmosphere at Paranal showing the deep absorption bands between the filters. Also shown is the spectrum of a G8V star (thick grey line) from the Pickles spectral library (Pickles 1998) along with a smoothed spectrum of ϵ Indi Ba (thick, black line). This highlights the difference between the fraction of each object's flux in the regions of high atmospheric absorption. Importantly, we see that the MKO filters mostly avoid these regions, while the ISAAC filters, especially the *J*-band, extend into them. Photometry using filters which extend into these regions are susceptible to variations in the atmosphere and mismatches between target and standard star spectra.

the old UKIRT *L*-band filter and was assumed to be unchanged on transformation to the MKO *L'*-band as for other A-type stars (see Fig. 2 of Leggett et al. 2003, and the UKIRT photometric calibration web-pages⁴), with the spread in the *L/L'* magnitude differences of A stars being used as an estimate of the uncertainty on the transformation. For the *M_{NB}*-band, the standard star magnitude was known in the ESO system of van der Bliek et al. (1996).

With the flux calibrated spectra of ϵ Indi Ba and Bb, we extracted synthetic photometry in the MKO *JHKLM'* filters and the 2MASS *JHK_S* filters by convolving the flux-calibrated spectra with the appropriate filter profiles and atmosphere for each site. In deriving our synthetic magnitudes, we used the ISAAC filters convolved with the model atmosphere given in the ISAAC user manual⁵ for typical conditions over Paranal. For the 2MASS magnitudes, we used the relative spectral responses of Cohen et al. (2003) and applied the zero-point offsets of +0.001, -0.019, +0.017 for the *J*, *H*, and *K_S*-bands respectively. The MKO filters used were convolved with the 1.2 mm PWV (precipitable water vapour) ATRAN model atmosphere of Lord (1992), as used by Stephens & Leggett (2004). We did not include the quantum efficiency of the detector nor the transmission profiles of any other optical elements. These were assumed to be practically flat across each near-IR filter as discussed in Stephens & Leggett (2004). However, although the reflectivity of aluminium (used to coat the VLT mirrors) is relatively constant across the near-IR⁶, we note that it is strongly wavelength-dependent in the optical regime. We therefore did

not attempt to derive our optical photometry in the same manner.

That said, the precise optical filters used significantly affect the derived photometry as the flux of a T dwarf rises by more than three orders of magnitude over the range 0.6–1.0 μm . Since our observed spectra do not cover the full *V*- and *R*-bands, we have not attempted to transform our optical photometry via synthetic photometry. Instead, we assumed that the magnitudes of our standard stars, as given by Landolt (1992) (*VRI* in the system of Bessell 1990) and SDSS (*z*), were the same as that in the FORS2 system as would be the case for an A0 star. The spread in derived zero-points for the different standard stars were smaller than the other uncertainties which leads us to believe that the precise spectral type of the standard stars did not significantly affect the derived photometry. However, our optical photometry of ϵ Indi Ba, Bb is not what would be measured through the standard Bessell filters and so is not readily compared with other T dwarf observations.

References

- Abia, C., Rebolo, R., Beckman, J. E., & Crivellari, L. 1988, A&A, 206, 100
Allard, F., Hauschildt, P., Alexander, D., Tamanai, A., & Schweitzer, A. 2001, ApJ, 556, 357
Allard, F., Guillot, T., Ludwig, H.-G., et al. 2003, in Brown Dwarfs, ed. E. Martín, IAU Symp., 211, 325
Allard, F., Allard, N. F., Homeier, D., et al. 2007, A&A, 474, L21
Appenzeller, I., Fricke, K., Fürtig, W., et al. 1998, The Messenger, 94, 1
Asplund, M., Grevesse, N., & Sauval, A. J. 2005, in Cosmic Abundances as Records of Stellar Evolution and Nucleosynthesis, ASP Conf. Ser., 336, 25
Ayles, T. R. 2008, ApJ, 686, 731
Baraffe, I., Chabrier, G., Allard, F., & Hauschildt, P. H. 1997, A&A, 327, 1054
Baraffe, I., Chabrier, G., Allard, F., & Hauschildt, P. H. 1998, A&A, 337, 403
Baraffe, I., Chabrier, G., Barman, T. S., Allard, F., & Hauschildt, P. H. 2003, A&A, 402, 701
Barber, R. J., Tennyson, J., Harris, G. J., & Tolchenov, R. N. 2006, MNRAS, 368, 1087
Barnes, S. A. 2007, ApJ, 669, 1167
Bendinelli, O., Parmeggiani, G., Piccioni, A., & Zavatti, F. 1987, AJ, 94, 1095
Bessell, M. S. 1990, PASP, 102, 1181
Bildsten, L., Brown, E. F., Matzner, C. D., & Ushomirsky, G. 1997, ApJ, 482, 442
Burgasser, A. J. 2007, AJ, 134, 1330
Burgasser, A. J. 2009, 1094, 501
Burgasser, A. J., Kirkpatrick, J. D., Reid, I. N., et al. 2000, AJ, 120, 473
Burgasser, A. J., Kirkpatrick, J. D., Brown, M. E., et al. 2002, ApJ, 564, 421
Burgasser, A. J., Kirkpatrick, J. D., Liebert, J., & Burrows, A. 2003, ApJ, 594, 510
Burgasser, A. J., McElwain, M. W., Kirkpatrick, J. D., et al. 2004, AJ, 127, 2856
Burgasser, A. J., Burrows, A., & Kirkpatrick, J. D. 2006a, ApJ, 639, 1095
Burgasser, A. J., Geballe, T. R., Leggett, S. K., Kirkpatrick, J. D., & Golimowski, D. A. 2006b, ApJ, 637, 1067
Burke, C. J., Pinsonneault, M. H., & Sills, A. 2004, ApJ, 604, 272
Burningham, B., Pinfield, D. J., Leggett, S. K., et al. 2008, MNRAS, 391, 320
Burningham, B., Pinfield, D. J., Leggett, S. K., et al. 2009, MNRAS, 395, 1237
Burrows, A. 2009 [arXiv:0902.1777]
Burrows, A., Marley, M., Hubbard, W. B., et al. 1997, ApJ, 491, 856
Burrows, A., Marley, M. S., & Sharp, C. M. 2000, ApJ, 531, 438
Burrows, A., Burgasser, A. J., Kirkpatrick, J. D., et al. 2002, ApJ, 573, 394
Burrows, A., Sudarsky, D., & Hubeny, I. 2006, ApJ, 640, 1063
Caffau, E., Ludwig, H.-G., Steffen, M., et al. 2008, A&A, 488, 1031
Cannon, R. D. 1970, MNRAS, 150, 111
Cardoso, C. V., McCaughrean, M. J., King, R. R., et al. 2009a, in AIP Conf. Ser., 1094, 509
Carpenter, J. M. 2001, AJ, 121, 2851
Chabrier, G., Baraffe, I., & Plez, B. 1996, ApJ, 459, L91
Chabrier, G., Baraffe, I., Allard, F., & Hauschildt, P. 2000, ApJ, 542, 464
Chiu, K., Fan, X., Leggett, S. K., et al. 2006, AJ, 131, 2722
Close, L. M., Lenzen, R., Guirado, J. C., et al. 2005, Nature, 433, 286
Close, L. M., Thatte, N., Nielsen, E. L., et al. 2007, ApJ, 665, 736
Cohen, M., Wheaton, W. A., & Megeath, S. T. 2003, AJ, 126, 1090
D'Antona, F., & Mazzitelli, I. 1994, ApJS, 90, 467
Diego, F. 1985, PASP, 97, 1209

⁴ http://www.jach.hawaii.edu/UKIRT/astrometry/calib/phot_cal/-ukirt_stds.html

⁵ <http://www.eso.org/sci/facilities/paranal/instruments/isaac/doc/>

⁶ http://www.gemini.edu/files/docman/press_releases/pr2004-5/images/comparison_AgAl_02.GIF

- Dupuy, T. J., Liu, M. C., & Ireland, M. J. 2009, *ApJ*, 692, 729
- Eggen, O. J. 1958, *MNRAS*, 118, 154
- Eggen, O. J. 1971, *PASP*, 83, 251
- Ferraro, F. R., Messineo, M., Fusi Pecci, F., et al. 1999, *AJ*, 118, 1738
- Franz, O. G. 1973, *JRASC*, 67, 81
- Freytag, B., Allard, F., Ludwig, H., Homeier, D., & Steffen, M. 2010, *A&A*, submitted
- Geballe, T. R., Knapp, G. R., Leggett, S. K., et al. 2002, *ApJ*, 564, 466
- Golimowski, D. A., Leggett, S. K., Marley, M. S., et al. 2004, *AJ*, 127, 3516
- Grevesse, N., & Noels, 1993, in *Abundances*, ed. C. Jaschek, & M. Jaschek (Dordrecht: Kluwer), 111
- Griffith, C. A., & Yelle, R. V. 1999, *ApJ*, 519, L85
- Hamuy, M., Suntzeff, N. B., Heathcote, S. R., et al. 1994, *PASP*, 106, 566
- Hauschildt, P. H., & Baron, E. 1999, *J. Comput. Appl. Math.*, 109, 41
- Hayes, D. S. 1985, in *Calibration of Fundamental Stellar Quantities*, ed. D. S. Hayes, L. E. Pasinetti, & A. G. D. Philip, *IAU Symp.*, 111, 225
- Helling, C., Ackerman, A., Allard, F., et al. 2008, *MNRAS*, 391, 1854
- Henry, T. J., Soderblom, D. R., Donahue, R. A., & Baliunas, S. L. 1996, *AJ*, 111, 439
- Hewett, P. C., Warren, S. J., Leggett, S. K., & Hodgkin, S. T. 2006, *MNRAS*, 367, 454
- Hinkle, K. H., Wallace, L., & Livingston, W. 2003, in *BAAS*, 35, 1260
- Homeier, D., Hauschildt, P., & Allard, F. 2003, in *Stellar Atmosphere Modeling, Proceedings of an International Workshop held 8–12 April 2002 in Tübingen, Germany*, ed. I. Hubeny, D. Mihalas, & K. Werner (San Francisco: ASP), *ASP Conf. Ser.*, 288, 357
- Kasper, M., Burrows, A., & Brandner, W. 2009, *ApJ*, 695, 788
- King, I. R. 1971, *PASP*, 83, 199
- Kirkpatrick, J. D., Cruz, K. L., Barman, T. S., et al. 2008, *ApJ*, 689, 1295
- Kirkpatrick, J. D., Reid, I. N., Liebert, J., et al. 2000, *AJ*, 120, 447
- Knapp, G. R., Leggett, S. K., Fan, X., et al. 2004, *AJ*, 127, 3553
- Koen, C. 2005, *MNRAS*, 360, 1132
- Koen, C., Tanabé, T., Tamura, M., & Kusakabe, N. 2005, *MNRAS*, 362, 727
- Kurucz, R. L. 2005, *Mem. Soc. Astron. Ital. Suppl.*, 8, 189
- Lachaume, R., Dominik, C., Lanz, T., & Habing, H. J. 1999, *A&A*, 348, 897
- Landolt, A. U. 1992, *AJ*, 104, 340
- Leggett, S. K., Hawarden, T. G., Currie, M. J., et al. 2003, *MNRAS*, 345, 144
- Leggett, S. K., Saumon, D., Albert, L., et al. 2008, *ApJ*, 682, 1256
- Leggett, S. K., Cushing, M. C., Saumon, D., et al. 2009, *ApJ*, 695, 1517
- Lenzen, R., Hartung, M., Brandner, W., et al. 2003, in *SPIE Conf. Ser.* 4841, ed. M. Iye, & A. F. M. Moorwood, 944
- Liu, M. C., Dupuy, T. J., & Ireland, M. J. 2008, *ApJ*, 689, 436
- Lodders, K., & Fegley, Jr., B. 2006, *Chemistry of Low Mass Substellar Objects, Astrophysics Update 2*, 1
- Looper, D. L., Kirkpatrick, J. D., & Burgasser, A. J. 2007, *AJ*, 134, 1162
- Lord, S. D. 1992, *NASA Tech. Memo.*, 103957
- Ludwig, H.-G., Allard, F., & Hauschildt, P. H. 2006, *A&A*, 459, 599
- Luhman, K. L., & Potter, D. 2006, *ApJ*, 638, 887
- Luhman, K. L., Stauffer, J. R., & Mamajek, E. E. 2005, *ApJ*, 628, L69
- Mainzer, A. K., Roellig, T. L., Saumon, D., et al. 2007, *ApJ*, 662, 1245
- Maiolino, R., Rieke, G. H., & Rieke, M. J. 1996, *AJ*, 111, 537
- Marois, C., Macintosh, B., Song, I., & Barman, T. 2005 [[arXiv:0502.382](https://arxiv.org/abs/0502.382)]
- McCaughrean, M. J., Close, L. M., Scholz, R.-D., et al. 2004, *A&A*, 413, 1029
- McLean, I. S., McGovern, M. R., Burgasser, A. J., et al. 2003, *ApJ*, 596, 561
- McLean, I. S., Prato, L., McGovern, M. R., et al. 2007, *ApJ*, 658, 1217
- Moffat, A. F. J. 1969, *A&A*, 3, 455
- Moorwood, A., Cuby, J.-G., Biereichel, P., et al. 1998, *The Messenger*, 94, 7
- Mountain, C. M., Selby, M. J., Leggett, S. K., Blackwell, D. E., & Petford, A. D. 1985, *A&A*, 151, 399
- Nielsen, E. L., Close, L. M., Guirado, J. C., et al. 2005, *Astron. Nachr.*, 326, 1033
- Noll, K., Geballe, T., & Marley, M. 1997, *Detection and Study of Planets Outside the Solar System*, 23rd meeting of the IAU, Joint Discussion 13, 25–26 August 1997, Kyoto, Japan, meeting abstract. 13
- Oke, J. B. 1990, *AJ*, 99, 1621
- Perryman, M. A. C., & ESA 1997, *The HIPPARCOS and TYCHO catalogues. Astrometric and photometric star catalogues derived from the ESA HIPPARCOS Space Astrometry Mission*, *ESA SP*, 1200
- Persson, S. E., Murphy, D. C., Krzeminski, W., Roth, M., & Rieke, M. J. 1998, *AJ*, 116, 2475
- Pickles, A. J. 1998, *PASP*, 110, 863
- Prinn, R. G., & Barshay, S. S. 1977, *Science*, 198, 1031
- Racine, R. 1996, *PASP*, 108, 699
- Reiners, A., Homeier, D., Hauschildt, P. H., & Allard, F. 2007, *A&A*, 473, 245
- Rocha-Pinto, H. J., Castilho, B. V., & Maciel, W. J. 2002, *A&A*, 384, 912
- Roellig, T. L., Houck, J. R., Van Cleve, J. E., et al. 1998, in *SPIE Conf. Ser.* 3354, ed. A. M. Fowler, 1192
- Roellig, T. L., Van Cleve, J. E., Sloan, G. C., et al. 2004, *ApJS*, 154, 418
- Rossow, W. B. 1978, *Icarus*, 36, 1
- Rousset, G., Lacombe, F., Puget, P., et al. 2003, in *SPIE Conf. Ser.* 4839, ed. P. L. Wizinowich, & D. Bonaccini, 140
- Saar, S. H., & Osten, R. A. 1997, *MNRAS*, 284, 803
- Santos, N. C., Mayor, M., Naef, D., et al. 2001, *A&A*, 379, 999
- Santos, N. C., Israelian, G., & Mayor, M. 2004, *A&A*, 415, 1153
- Saumon, D., & Marley, M. S. 2008, *ApJ*, 689, 1327
- Saumon, D., Marley, M. S., Lodders, K., & Freedman, R. S. 2003, in *IAU Symp.*, 345
- Schilbach, E., Röser, S., & Scholz, R.-D. 2009, *A&A*, 493, L27
- Scholz, R.-D., McCaughrean, M. J., Lodieu, N., & Kuhlbrodt, B. 2003, *A&A*, 398, L29
- Smith, V. V., Tsuji, T., Hinkle, K. H., et al. 2003, *ApJ*, 599, L107
- Soubiran, C., & Girard, P. 2005, *A&A*, 438, 139
- Sousa, S. G., Santos, N. C., Mayor, M., et al. 2008, *A&A*, 487, 373
- Stephens, D. C., & Leggett, S. K. 2004, *PASP*, 116, 9
- Sterzik, M. F., Pantin, E., Hartung, M., et al. 2005, *A&A*, 436, L39
- Stetson, P. B. 1987, *PASP*, 99, 191
- Tokunaga, A. T., Simons, D. A., & Vacca, W. D. 2002, *PASP*, 114, 180
- Tsuji, T. 2002, *ApJ*, 575, 264
- van der Bliek, N. S., Manfroid, J., & Bouchet, P. 1996, *A&AS*, 119, 547
- van Leeuwen, F. 2007, *A&A*, 474, 653
- Wallace, L., Livingston, W., Hinkle, K., & Bernath, P. 1996, *ApJS*, 106, 165
- Yung, Y. L., Drew, W. A., Pinto, J. P., & Friedl, R. R. 1988, *Icarus*, 73, 516